Structure, Electronic Properties, Morphology Evolution, and Photocatalytic Activity in PbMoO₄ and Pb₁₋₂ₓCaₓSrₓMoO₄ (x= 0.1, 0.2, 0.3, 0.4 and 0.5) Solid Solutions

E.O. Gomes[1], L. Gracia[1,2], A.A.G. Santiago[3], R.L.Tranquilin[4], F.V. Motta[3], R.A.C. Amoresi[1,5], E. Longo[4], M.R.D. Bomio[3], J. Andres[1*].

[1]*Department of Analytical and Physical Chemistry, Universitat Jaume I, 12071 Castelló, Spain*

[2]*Permanent address: Department of Physical Chemistry, University of Valencia (UV), 46100 Burjassot, Spain*

[3]*LSQM – Laboratory of Chemical Synthesis of Materials – Department of Materials Engineering, Federal University of Rio Grande do Norte – UFRN, P.O. Box 1524, Natal, RN, Brazil*

[4]*CDMF-LIEC, UFSCar, P.O. Box 676, 13565-905 São Carlos, SP, Brazil*

[5]*School of Engineering, Sao Paulo State University (UNESP), Guaratinguetá, São Paulo 12516-410, Brazil*

ABSTRACT

In this work PbMoO₄ and Pb₁₋₂ₓCaₓSrₓMoO₄ (x= 0.1, 0.2, 0.3, 0.4 and 0.5) solid solutions have been successfully prepared, for the first time, by a simple co-precipitation method and the as-synthesized samples were subjected to a water-based reflux treatment. Structural characterization of these samples was performed using X-ray diffraction with Rietveld refinement analysis and Raman spectroscopy. Their optical properties were investigated by UV–Vis absorption spectroscopy and PL emissions, and the photocatalytic activity of the as-synthesized samples for the degradation process of Rhodamine B has been demonstrated. The surface structure and morphologies were characterized by field emission scanning electron microscopy. To complement and rationalize the experimental results, the geometry, electronic structures, and

morphologies of as-synthesized samples were characterized by first-principles quantum-mechanical calculations at the density functional theory level. By using Wulff construction, based on the values of the surface energies for the (001), (100), (110), (111), (011) and (112) surfaces, a complete map of the available morphologies for $PbMoO_4$ was obtained and a good agreement between the experimental and theoretical predicted morphologies were found. The structural and electronic changes induced by the substitution of Pb by Ca and Sr allow us to find a relationship among morphology, the electron-transfer process at the exposed surfaces, optical properties, and photocatalytic activity. We believe that our results offer new insights regarding the local coordination of superficial Pb/Ca/Sr and Mo cations (i.e., clusters) on each exposed surface of the corresponding morphology, which dictate the photocatalytic activities of the as-synthesized samples, a field that has so far remained unexplored. The present study, which combines multiple experimental methods and first-principles calculations, provides a deep understanding of the local structures, bonding, morphologies, band gaps, and electronic and optical properties, and opens the door to exploit the electrical, optical and photocatalytic activity of this very promising family of materials.

Corresponding author: J. Andrés*. E-mail address:* andres@qfa.uji.es.

1. Introduction

Metal molybdates have aroused great interest due to their broad applications in a wide range of technological fields such as catalysts and photocatalysis, optics, magnetism, gas sensors and electrochemistry [1-12]. Among the metal molybdates, the $AMoO_4$ (A = Ca, Sr, Ba and Pb) family with a scheelite structure and spatial group *I41* presents excellent photoluminescent and photocatalytic properties [13-16], lead molybdate, $PbMoO_4$ (PMO), being one of the most promising compounds in this family [5]. It is organized structurally by two fundamental units with point of symmetry S4 [6]. The larger, Pb^{2+}, and smaller, Mo^{6+}, cations are coordinated by eight and four oxygen atoms, forming a cluster with a dodecahedral arrangement, $[PbO_8]$, and a cluster of tetrahedral arrays $[MoO_4]$, respectively [7]. The valence band (VB) consists of the hybridization of O *2p* and Pb *6s* orbitals, while the conduction band (CB) is composed mainly of Mo *4d* orbitals, the band gap between CB and VB being approximately 3.2 eV [8]. PMO is employed as photocatalysts [9], semiconductor material [10] and an antibacterial agent [11].

Different synthetic procedures have been employed to obtain PMO, such as the solid state reaction [12]; the electrochemical method [13]; combustion synthesis [14]; polymerization of complexes [15]; reverse micro emulsion [16]; citrate complex method [17], solvothermic synthesis [18], conventional hydrothermal [11] and the hydrothermal microwave assisted methods [19]. Some of these methods, however, offer disadvantages, such as the generation and formation of organic residues, prolonged synthesis times, and high energy release. Other synthesis methods are therefore needed to overcome these drawbacks. The water-based reflux method is a simple, inexpensive, and easily applicable process [20]. It has already been used for the synthesis of nanoparticles [21], nanotubes [22], nano-shell structures and nanowires [23]. It is well known that the properties of the as-synthesized samples are highly dependent on the synthesis method and thermal

treatments. The size, morphology and crystallinity of the desired nanostructures can be controlled by varying the reaction time, concentration of the precursors, and the type of solvent used.

The synthesis of solid solutions offers the advantage of the continuous change of properties with components, which is a very effective strategy to tune the properties of advanced materials with extended functionalities. Continuous series of substitutional solid solutions can provide a variation in crystal structure and changes in the band gap values and optical properties, and an opportunity to understand the structure property relationship can thus be achieved [24][25]. The design of a solid solution based on molybdate compounds is a promising strategy for developing novel materials [26], with the aim of improving their properties, and consequently expansion wider range of applications [27][28][29]. In particular, Hallaoui et al. [30] have studied the structural and optical properties as a function of composition x for $Sr_{(1-x)}Pb_xMoO_4$ solid solutions, showing that the photocatalytic activity of PMO and $SrMoO_4$ is different despite the similarity of the structures. In this context, our research group has been engaged in a research project devoted to the study of the structural, morphological, and optical properties of different solid solutions of wolframite- and tungstate-based materials by using a combination of first principles calculations and experimental techniques [24][31][32].

This work reports a series of new solid solutions with improved stability, which are appealing materials for several applications. Inspired by the above considerations, in this study, we seek to fulfill a four-fold objective. The first is to report, for the first time, on the synthesis of PMO and $Pb_{1-2x}Ca_xSr_xMoO_4$ (x= 0.1, 0.2, 0.3, 0.4 and 0.5 (CSMO)) solid solutions by employing the co-precipitation method, followed by a water-based reflux treatment. This synthesis method is a simple, low-cost, and easy synthesis

procedure that has received special attention due to the fact that it allows the formation of oxides with a high degree of crystallinity and easy dispersion in aqueous medium, reduced reaction times, low synthesis temperatures, excellent control of reaction parameters, control of product size and morphology, and enhanced product purity or material properties. Secondly, X-ray diffraction (XRD), field emission electron microscopy (FE-SEM), Micro Raman (MR) and ultraviolet-visible (UV-Vis) spectroscopies were employed to characterize the samples and determine the effect of their chemical composition on the morphology and photoluminescence (PL) emissions. The third aim is to complement and rationalize experimental results by means of first principles calculation, at the density functional theory (DFT) level, to obtain the geometry, electronic structure, and properties of PMO and the solid solutions. The fourth aim is to apply a joint experimental and theoretical strategy that we developed in order to obtain a complete map of the morphologies. From these results, we hope to understand how the different surfaces change their energies throughout the synthesis process and propose a mechanism by which the experimental and theoretical morphologies of the solid solutions match. Finally, the insights gained through these calculations help to rationalize the mechanism and origin of the photocatalytic activity on the degradation process of Rhodamine B (RhB) dye. We discuss how knowledge of surface-specific properties can be utilized to design a number of crystal morphologies that may offer improved performance in various applications. The different activities can be associated to the presence of the number of unsaturated superficial Pb/Sr/Ca and Mo cations capable of forming the main active adsorption sites. We believe that these novel results are of significant relevance, since they may inspire the efficient synthesis of these and related molybdate solid solutions and provide critical information to expand our fundamental understanding, while also perhaps contributing to the rational design of new materials for multifunctional applications.

This paper contains three more sections. The next section describes the experimental and theoretical procedures, with the synthesis and characterization, as well as the computational methods and model systems. In section three, the results are presented and discussed. The main conclusions are summarized in the fourth and final section.

2. Experimental and theoretical procedures

2.1. Materials

Calcium nitrate hexahydrate [$Ca(NO_3)_2 \cdot 4H_2O$] (98.0% purity; Vetec), strontium nitrate [$Sr(NO_3)_2$] (99.0% purity, Vetec), molybdic acid [H_2MoO_4] (85% purity; Alfa Aesar), ammonium hydroxide (NH_4OH), and distilled water were used as reagents to prepare the $Pb_{1-2x}Ca_xSr_xMoO_4$.

2.2. Synthesis of PMO and $Pb_{1-2x}Ca_xSr_xMoO_4$ powders

Powder samples of PMO and $Pb_{1-2x}Ca_xSr_xMoO_4$. (x= 0.1, 0.2, 0.3, 0.4 and 0.5) were prepared by using the reflux method. The synthesis procedure is described as follows: Molybdic acid (5.0×10^{-3} mol) was dissolved in 50 ml deionized water (solution 1). At the same time, the respective concentrations (% mol) of lead, calcium, and strontium nitrates were dissolved in 50 ml deionized water (solution 2). Solution 2 was added dropwise to solution 1 and the pH of the solution was adjusted to 11 by adding ammonium hydroxide to it, and the formation of a white precipitate was observed. Afterward, this solution was stirred for 30 min in an ultrasound bath to accelerate the co-precipitation rate. Subsequently, this preformed mixture was transferred to a 150 ml round-bottomed flask and refluxed at 100°C / 1h.

The resulting precipitate was washed several times with deionized water to neutralize the suspension (pH ≈7). Finally, the white precipitates were collected and dried

at 80°C/24 hours. The samples were named according to the concentration of Pb^{2+} cations, i.e., the names of the samples are defined for each value x of the substituents (Ca^{2+}/Sr^{2+}) and the corresponding amount of Pb^{2+}: x= 0, 0.1, 0.2, 0.3, 0.4 and 0.5. Hence, they were given the denominations PMO, Pb0.8, Pb0.6, Pb0.4, Pb0.2 and CSMO, respectively.

2.3. Characterization of $Pb_{1-2x}Ca_xSr_xMoO_4$ samples

XRD patterns of the PMO and $Pb_{1-2x}Ca_xSr_xMoO_4$ samples were collected within the 10º to 120º angular range with a step speed of 0.02° min^{-1} using an XRD 7000 Shimadzu diffractometer and monochromatic Cu K$_\alpha$ (λ = 1.5406 Å) radiation. The powder morphology was examined using an FE-SEM (Carl Zeiss, model Supra 35-VP) operating at 6 kV. Micro Raman (MR) spectroscopy was conducted on a Horiba Jobin-Yvon (Japan) spectrometer coupled to a charge-coupled device detector and Ar-ion laser (MellesGriot, United States) operating at 514.5 nm with a maximum power of 200 mWMR, and measurements were recorded using a T-64000 spectrometer (Jobin-Yvon, France) triple monochromator coupled to a CCD detector. The UV-Vis reflectance spectrum was obtained using a UV-Vis spectrometer (Shimadzu, model UV-2600). PL spectra were measured using a Thermal Jarrell-Ash Monospec 27 monochromator and a Hamamatsu R446 photomultiplier. The excitation source used was a krypton laser with a wavelength of 325 nm (Coherent Innova) and an output of approximately 13.3 mW. The photon energies with the emitted wavelengths were calculated based on Planck-Einstein equation (1), where E is the photon energy, in eV, and λ the photon wavelength, in nm.

$$E = \frac{1240}{\lambda} \qquad (1)$$

The photocatalytic properties for the degradation of Rhodamine B (RhB) dye in an aqueous solution were tested under UV-light illumination. About 50 mg of catalyst crystals were placed in a 150 mL beaker, and 50 mL of RhB solution (1×10^{-5} mol L^{-1})

was added. These suspensions were ultrasonicated for 10 min in an ultrasonic cleaner before illumination. UV illumination was then performed by placing the solution under six UVC lamps (15 W TUV Philips, with maximum intensity of 254 nm = 4.9 eV).

2.4. Computational methods and model systems

The structural and electronic properties of the PMO structure and $Pb_{1-2x}Ca_xSr_xMoO_4$ solid solutions were calculated using Becke's three-parameter hybrid non-local exchange *functional*, combined with a Lee-Yang-Parr gradient-corrected correlation functional (B3LYP), implemented in the CRYSTAL17 package [33]. The atoms were centered and described using pseudopotential databases Ca_pob_TZVP_2012,Sr_ECP28MDF_s411p411d11_Heifets_2013,Pb_ECP60MDF_doll_2011, 976-311 (d631) G and O-6-31G* (all-electron) for Ca, Sr, Pb, Mo and O, respectively. Regarding the diagonalization of the density matrix, the reciprocal space net was described by a shrinking factor of 4, generated according to the Monkhorst–Pack scheme. The accuracy of the evaluation of the Coulomb and exchange series was controlled by five thresholds, whose adopted values were 10^{-8}, 10^{-8}, 10^{-8}, 10^{-8}, and 10^{-16}.

The representation of the PMO and CSMO bulk structure is shown in Figure 1. Mo atoms are coordinated to four O atoms, and the local coordination can be described by a tetrahedral [MoO$_4$] cluster. Correspondingly, the Pb, Ca and Sr are coordinated to eight O atoms, resulting in a formation of [PbO$_8$], [CaO$_8$] and [SrO$_8$] clusters, respectively. To simulate the substitution process and to obtain the ideal percentages presented in the experimental data, a 5x1x1 supercell, with a volume 5 times larger than the primitive cell and 60 atoms was used. The most stable distribution of Pb, Ca, and Sr atoms in the $Pb_{1-2x}Ca_xSr_xMoO_4$ solid solutions Pb0.8 (x=0.1), Pb0.6 (x=0.2), Pb0.4 (x=0.3) and Pb0.2 (x=0.4) can be seen in Figure S1. We have computed the formation

energy (ΔE_f) of each system, PMO and $Pb_{1-2x}Ca_xSr_xMoO_4$ solid solutions, using the following formula:

$$\Delta E_f = \frac{E_f - (vE_{Pb} + wE_{Mo} + xE_O + yE_{Ca} + zE_{Sr})}{(v+w+x+y+z)} \tag{2}$$

where E_f is the total energy of a system, $E_{Pb}, E_{Mo}, E_O, E_{Ca}$ and E_{Sr} denote the total energy per atom of pure elements in their stable crystal structures indicated as subscripts, and *v, w, x, y, z* are the numbers of the corresponding atoms, respectively.

The values of the surface energy, E_{surf}, of the (001), (100), (110), (111) and (112) surfaces were obtained. E_{surf} is defined as the total energy of the repeating slab (E_{slab}) minus the total energy of the perfect crystal per molecular unit (E_{bulk}) multiplied by the number of molecular units of the surface (N) and divided by the surface area per repeating cell of the two sides of the slab:

$$E_{surf} = \frac{1}{2A}(E_{slab} - NE_{bulk}) \tag{3}$$

In this work, after the optimization process and convergence tests on thickness, slab models consisting of 10 molecular units containing 60 atoms were obtained. In addition, the relaxation process was performed, with the relaxed energy (E_{relax}) being calculated as the difference between the total energies for relaxed and unrelaxed slabs, as follows:

$$E_{relax} = \frac{(E_{slab}^{unrlx} - E_{slab}^{relax})}{2A} \tag{4}$$

The E_{slab}^{unrlx} and E_{slab}^{relax} correspond to the total energies for the unrelaxed and relaxed slab models, respectively.

In addition, the broken bonding density (D_b), defined as the number of broken bonds per unit cell area when a surface is created, can be calculated by using equation 5 [34][35].

$$D_b = \frac{N_b}{A} \qquad (5)$$

where N_b is the number of broken bonds per unit cell area on a specific surface and A is the unit of the surface area. From the D_b values that were calculated, it is possible to predict the order of surface stability, since it has been established that higher values are obtained when a larger number of defects are present on the surface[36].

By using the Wulff construction, the E_{surf} at a fixed volume is minimized, thereby providing a simple correlation between the surface energy of the (hkl) plane and the distance (rhkl) in the normal direction from the center of the crystallite [37]. The procedure to obtain the complete set of morphologies has been presented previously by Andrés et al [38], and it has been successfully used in materials science to obtain the morphology of materials, including PMO [39], $CaWO_4$ [40], Ag_3PO_4 [41], α-Ag_2MoO_4 [42], $BaMoO_4$ [43], $BaWO_4$ [44], Ag_2CrO_4 [45] and $LaVO_4$ [46].

3. Results and Discussion

3.1. X-ray diffraction

The XRD patterns of the as-synthesized samples are shown in Figure 2. Well defined peaks are observed, indicating good crystallinity and long-range structural order without the presence of secondary phases. Being in accordance with the profile and the standards for PMO, indexed to JCPDS 44-1486, the tetragonal structure of the scheelite type and space group I41/a is obtained. However, the Ca^{2+} and Sr^{2+} cation replacement processes in the PMO matrix induce an increase in peaks and a main peak unfolding of the samples, starting with sample Pb0.6 and changing to a larger angle (see Figure 2),

which may be associated with the difference in the size of these cations. A similar result was obtained by Song et al. along the Cr^{3+} cation substitutions in the PMO matrix [8].

For comparison purposes, the values of the bond lengths, the volume, and the cell parameters have been reported in Tables 1 and 2. A good agreement between experimental and theoretical values can be observed for PMO and CSMO sample, revealing a reduction in the cell volume proportional to the molar concentration of the dopants added. This behavior, more pronounced in theoretical than in experimental data, (see Table 2) can be associated to the different values of bond distances, M-O (M= Mo, Ca, Sr), at the [MoO_4], [CaO_8], and [SrO_8] clusters due to changes in the atomic positions of the oxygen atoms [24]. Similar trend is reported by Hallaoui et al. for the $Sr_{(1-x)}Pb_xMoO_4$ solid solution, in which there is an increase in the Mo-O and M-O bond lengths at clusters (MoO_4) and (MO_8) (M = Sr/Pb) with increasing Pb^{2+} concentration [30].

The negative calculated values of formation energy per unit volume for PMO and solid solution structures according to equation (1) show that all of them are stable structures with values of -0.128, -0.217, -0.306, -0.396, -0.485 and -0.575 Hartree for PMO, Pb0.8, Pb0.6, Pb0.4, Pb0.2 and CSMO, respectively. The ΔE_f values calculated for the $Pb_{1-2x}Ca_xSr_xMoO_4$ solid solutions are found to increase monotonously with the Ca/Sr content, which is consistent with the process of continuous cation substitution from PMO to CSMO.

3.2. MR spectroscopy

Figure 3 shows the MR spectra in the range of 50 to 1050 cm^{-1}. The PMO is a structure that presents 13 active Raman vibrational modes, which can be described by equation (6). A and B are non-degenerate modes and E are doubly degenerate modes [47].

$$\Gamma = 3A_g + 5B_g + 5E_g \qquad (6)$$

In Figure 3a seven Raman vibration modes are found in the PMO matrix spectrum. The peak identified at $\sim$860 cm^{-1} as $\upsilon1$ (A_g) is associated with a characteristic symmetric stretching pattern of the molybdates. The peaks at approximately 760 and 740 cm^{-1} can be considered as corresponding to vibrational modes of the antisymmetric stretches $\upsilon3$ (B_g) and $\upsilon3$ (E_g), respectively. The peaks corresponding to 345 and 310 cm^{-1} were marked as $\upsilon4$ (E_g) and $\upsilon2$ (B_g, A_g), which correspond to antisymmetric and symmetric stretching of the $[MO_4]^{2-}$ group. The modes at 160 and 100 cm^{-1} were identified as A_g and E_g, corresponding to the rotational and translational modes, respectively.

All the samples showed the same MR spectrum profiles, which are also in agreement with the molybdate structure, and in particular PMO [48][49]. However, a shift in the spectra to larger wavenumbers is also observed, and the appearance of two other peaks, at 785 and 840 cm^{-1}, can be observed, mainly in $Pb_{1-2x}Ca_xSr_xMoO_4$ samples with x=0.5 (CSMO) and x=0.4 (Pb0.2), as shown in Figure 3b. Both peaks are also characteristic of $CaMoO_4$ and $SrMoO_4$ compounds [50]. The above results are thus a sign of the complete substitution of the Pb cations by the Ca and Sr cations in the samples.

Figures S2a and S2b in the supporting information (SI) display a comparison of the theoretical and experimental Raman modes. A good agreement can be seen, although there are a large number of theoretical Raman modes in relation to the experimental data. This is explained by the fact that these modes are not easily detected by experimental techniques due to their low intensities.

3.3. FE-SEM images

Figure 4 presents the FE-SEM images of the as-synthesized samples. Different particles sizes appear and a progressive evolution of agglomerated is observed as x=

(Ca/Sr) increases. It is observed that the PMO sample presents well dispersed anisotropic microcrystals with an octahedron-type morphology. Particles with octahedron-type morphology have been found in previous work [51], using a capping agent. In this work, without the presence of capping agents, only the synthesis method and the Ca/Sr substitution processes are responsible for the change in morphology and size. In addition, the presence of octahedra is dependent on the substitution of the Pb in the matrix, i.e., with a lower concentration of Pb, the number of well-defined octahedra decreases (Figures 4d-4f). A nanometric size of particles is observed for samples Pb0.8 and the particle shape changes according to the higher proportion of substitution of Pb cations, the octahedron-type morphology becomes more isotropic (Figures 4c and 4d) and there is a predominance of elongated nanoparticle morphologies (Figures 4e and 4f).

A deep insight to explain the changes in morphology can be provided by applying the Wulff construction based on the values of E_{surf}. Figure 5 shows the calculated E_{surf} values of PMO and solid solutions. The stability order of the surfaces is (001) < (011) < (112) < (110) < (100) < (111) for the PMO. For the CSMO system, there is an inversion in the order of stability between the (011) and (112) surfaces and between the (100) and (111) surfaces (Figure S3). In the solid solutions the change in the order stability involves the (100) and (111) surfaces, except for the system $Pb_{1-2x}Ca_xSr_xMoO_4$ with x=0.2.

The relative stability of the exposed surfaces with the Sr cation instead of the Ca cation yields similar results in the E_{surf} values that are associated with their structural and electronic properties, i.e., the arrangement of the atoms at the exposed surfaces. An analysis of the geometry of the studied surfaces suggests that all of them are O- and Pb-ended (see Figure 6) and the atomic arrangement of the atoms on the top of each surface result in the (001) and (112) surfaces presenting exposed undercoordinated $[PbO_6]$ clusters and complete $[MoO_4]$ clusters. The use of the Kröger-Vink notation [52] allows

us to analyze the number of Pb−O breaking bonds in the exposed clusters and then the superficial clusters can be written as $[PbO_6...2V_o^x]$, V_o^x being the oxygen vacancies. However, in the (100), (110), (011) and (111) surfaces there are undercoordinated $[PbO_5]$ clusters associated with the presence of three oxygen vacancies $[PbO_5...3V_o^x]$. In addition, there is a correlation between the surface stability and the N_b values, the number of Pb−O breaking bonds in the incomplete clusters at the exposed surfaces. The D_b values are also directly linked to the order of the surface energy stability, i.e., higher values of D_b represent a large number of defects on the surface and a higher surface energy value. Table S1 lists the surface area values and the calculated N_b and D_b values. In addition, the values of the surface bonds for PMO and $Pb_{1-2x}Ca_xSr_xMoO_4$ (Pb=0.2, Pb0.4, Pb0.6, Pb0.8 and CSMO) solid solutions are reflected in Table S1. The (001), (011) and (112) surfaces have similar values of E_{surf}, i.e., 0.388, 0.395 and 0.413 $J \cdot m^{-2}$, respectively, while low values of $N_b = 2$, 3 and 4, and $D_b = 6.56$, 8.09 and 7.05 nm^{-2}, respectively, can be sensed. The (110), (100) and (111) surfaces display the following order of stability: $0.52 < 0.56 < 0.60$ $J \cdot m^{-2}$, respectively, with values of $N_b = 4$, 6, and 7, and higher values of $D_b = 8.37$, 8.88 and 6.97 nm^{-2}, respectively. For the (111) surface, a correlation between the surface stability and D_b values is not found due to the large surface area. For the (011) surface, different slab cuts can be performed, the most stable being the symmetric one shown in Figure 6. In addition, some studies reported another non-symmetric slab cut with exposed $[MO_6]$ clusters, which present less stability ($\Delta E_{surf} = 0.25$ J/m^2) [44][53]. For the solid solutions $Pb_{1-2x}Ca_xSr_xMoO_4$, the number of Pb−O breaking bonds in the superficial clusters is maintained (as well as the D_b values), as can be seen in Figure S4.

Different crystal morphologies can be achieved by tuning the E_{surf} values of the different surfaces. Based on that, it was possible to obtain the map of the available morphologies (Figure 7), and to correlate with the experimental FE-SEM images. This

map shows the available morphologies of the PMO crystals and solid solutions starting with the ideal morphology (a) (bottom of Fig. 7). As (001) E_{surf} increases to 0.65 J/m^2, the morphology (b) is obtained with a faceted octahedron defined mainly by the (001), (011) and (112) surfaces, similar to that found experimentally for the PMO sample. In addition, morphology (b) is in agreement with other previous works where the co-precipitation method was employed for the synthesis of PMO [54]. On the other hand, the simultaneous increase of the (001) and (112) E_{surf} values to 0.80 J/m^2 results in the morphology (c) with the main presence of (011) surface (left side bottom in Fig. 7), similar to that found for the Pb0.8 sample. By decreasing the E_{surf} of (110) surface to 0.23 J/m^2, the octahedron-type morphology becomes more elongated allowing (110) surface to be exposed in the resulting morphology (d), which can match to the Pb0.6 sample, showed in Figure 4(c).

3.4. Electronic Properties

3.4.1. UV-Visible Spectroscopy

Diffuse reflectance spectroscopy was used to obtain the band gap energy (E_{gap}) of the samples and the reflectance spectra were converted to absorbance using the Kubelka-Munk function, given by equation (7) [55].

$$F(R_\infty) = \frac{(1-R_\infty)^2}{2R_\infty} = \frac{K}{S} \tag{7}$$

where $F(R_\infty)$ is the Kubelka-Munk function or absolute reflectance of the sample; R_∞ is the diffuse reflectance; K is the molar absorption coefficient, and S is the scattering coefficient.

E_{gap} values were estimated using the Wood and Tauc [56] method and plotted in Figure S5. This method proposes that E_{gap} is related to the absorbance and energy of the photon, given by equation (8):

$$\alpha hv = C_1(hv - E_{gap})^n \tag{8}$$

where α is the linear absorption coefficient; hv is the photon energy; C_1 is a proportionality constant and n is indicated for different transitions ($n = 1/2$, 2, 3/2 or 3 for direct permission, indirect permission, prohibited direct, and indirect prohibition, respectively). The molybdates in general, which have a tetragonal structure of the scheelite type, allow direct electronic transitions ($n = 1/2$) [57][58].

The values of E_{gap} are dependent on the synthesis method, presence of defects, shape and size of the crystallite, structural and electronic modification in the lattice, and so on. In the metallic molybdates the corresponding emissions occur from charge transfer processes within $[MO_4]^{-2}$ units. In addition, the intermediate levels of energies generated from defects caused by the displacement of oxygen in the structure (vacancies) are associated with the order-disorder degree of these nanostructures [59][60].

The values of the E_{gap} of the samples are presented in Table S2 of the SI. Experimental and theoretical E_{gap} values obtained as a function of Pb content in $Pb_{1-2x}Ca_xSr_xMoO_4$ solid solution are displayed in Figure 8. An analysis of the results yields a similar behavior between experimental and theoretical results. However, it can be seen that experimental values are 9-15% smaller than those determined from calculations. Such differences are due to a well-known over-estimation in the E_{gap} values obtained with the B3LYP method which can explain the discrepancy with experiments. It is observed that the sample CSMO presents a high value of $E_{gap} = 4.03$ eV, while the PMO has a lower value (3.35 eV), in agreement with previous reports [7]. In general, molybdates present a high E_{gap}, since few intermediate levels between VB and CB are present [50][61].

However, in the solid solutions for values of x= 0.1, 0.2, 0.3 and 0.4, changes in the system and formation of transient structures occur, implying higher E_{gap} values as x is increased. In addition, Table S3 of the SI shows the E_{gap} values obtained for surfaces, where a similar behavior is obtained with bulk results. However, the E_{gap} value of the (100) surface remains almost constant.

3.4.2. Band structures, density of states and charge density maps

The valence band (VB) and conduction band (CB) of molybdates are mainly formed by the *2p* O and *4d* Mo states, respectively. As can be seen in Figure 9, for PMO the upper part of VB is also composed of the *6s* states of Pb hybridized with the *2p* state of O, while the lower part of CB is formed mainly by the *4d* states of Mo and *6p* states of Pb. The band structure of the CSMO sample is similar to $SrMoO_4$ and $CaMoO_4$ structures reported in the literature [62][63][64], in which the upper part of VB is composed by *2p* states of the O while the *4d* states for the Mo and *2p* of the O are predominant in the CB, with little contribution of the *3d* states of the Sr and *4d* states of the Ca in the upper part of CB.

An analysis of the band structures and density of states (DOS) of the PMO and CSMO systems presented in Figure 9 shows that their electronic structures differ. The band structure of the PMO shows an indirect band gap value of 3.61 eV, while CSMO presents a direct larger band gap value of 4.74 eV. In addition, both VB and CB of PMO are more dispersed than those of CSMO. Therefore, the *6s* orbitals of Pb contribute to raising the VB resulting in a narrower band gap of PMO compared with that of CSMO [65]. This difference may be associated with a higher charge density of the Pb cation compared to Sr/Ca cations. The presence of Pb cation states in the vicinity of the band gap influences the optical and luminescence properties of $PbMoO_4$. In particular, it has been found that the hole self-trapping at $[MoO_4]^{2-}$ anion, which is typically observed in

molybdates, is not possible in $PbMoO_4$ because holes can migrate along the *6s* Pb states located at the top of the VB[66][67].

The charge density maps are presented in Figure 10 with the aim of explaining electron density differences. Figures 10a and 10b show electron density maps for the PMO and CSMO, respectively, with a chosen plane (100) containing the Pb/Ca/Sr, Mo and O atoms. The high and low electron density zones on each map are represented by a different color in atomic units (electron/bohr^3), the area of accumulation of electron density being depicted in red, while the depletion zones of electron density are marked in blue. Thus, as expected, there is a higher electronic density around the Pb cations in relation to the Ca and Sr cations. Therefore, the higher dispersion of electronic density around the Pb cation contributes to the higher total density of the PMO promoted by the hybridization of the *6p* Pb and *2p* O orbitals, which is called "split-off hybridization" [65]. This fact allows PMO to have a larger charge mobility, lower recombination rate (electron-hole), and greater dispersion in its bands, resulting in lower E_{gap} values of PMO compared to CSMO [68][64]. The electron density isosurfaces (electron /bohr^3) for PMO and CSMO are shown in Figures 10c and 10d, respectively.

To verify the differences and contribution of each band, the DOS projected on atoms and orbitals for $Pb_{1-2x}Ca_xSr_xMoO_4$ structures with x=0.4 (Pb0.2), x=0.3 (Pb0.4), x=0.2 (Pb0.6) and x=0.1 (Pb0.8) are presented in Figure 11. It can be seen that the VB in all the structures are composed of O *2p* orbitals, Mo *4d*, and a low contribution of the Pb/(Ca, Sr) cations.

3.5. PL measurements

Figure 12a shows the PL spectra obtained with excitation at 325 nm at room temperature. The samples spectra displayed broadband emission behavior, with an

increase in the intensity of PL emission from the PMO sample to the Pb0.4 sample followed by a decrease in the intensity for the Pb0.2 and CSMO samples, as can be seen in Figure 12. The literature offers diverse explanations on the nature of the PL emissions in molybdates: i) The PL emission processes are associated to the transitions that occurs within $[MoO_4]^{2-}$ moiety, among the fundamental and excited electronic states [69][1][70]. The corresponding ground state has the $^1A_1$ symmetry, and the lowest excited states present $^1T_2$, $^1T_1$, $^3T_2$, and $^3T_1$ symmetries [64][71]. The transition $^1A_1 \leftrightarrow ^1T_2$ is a dipole-allowed transition, and lowest excited states $^3T_1$ and $^3T_2$ to the ground $^1A_1$ state are responsible for the material intrinsic luminescence, Figure 12b. The luminescence in this case would reveal emission bands referring to sub-levels between the triplet states $^3T_1$ and $^3T_2$ (region of 400 to 600 nm) due to the Jahn-Teller effect on the symmetry of the $[MoO4]^{2-}$ moiety [71], ii) From a structural and electronic point of view, the high concentration of defects favors the structural disorder at short range of $[MoO_4]^{2-}$ moiety, associated to the presence of oxygen vacancies, and the formation of intermediary energy level into the band gap, enhancing the probability of non-radioactive transitions and, consequently, increasing the suppression of the PL emission. [72][73][5][39]. In our work, the samples obtained by the reflux method are structurally ordered in long and disordered at short range, according to the XRD, MR spectroscopy and diffuse reflectance analyses (3.1, 3.2 and 3.4.2 sections). About the PL emission intensity was observed that the Pb0.4 and Pb0.6 samples display highest intensity whereas samples Pb0.8, Pb0.2 and PMO have the lowest intensities. Since the intensity of PL is related to the emission of radiation with low non-radioactive states, it can be inferred that samples with higher intensities of PL have less concentration of these states. In this sense, this is strongly related to the shorter values of the Mo-O bond distances, Table 2, due to the main clusters of surfaces exposed in these materials $[MO_6 ... 2V_O^x]$ (M: Pb or Ca), Figure 6. Then, PL

emission and the bonding distance are related to the amount and type of defects present in the structure [74].

Luminescent emission in oxides with high defects density occurs by several paths related to the high density of electronic states within the band gap, and this result in broad band characteristic. [58]. It is commonly referred to as shallow and deep defect type in the band gap that result in different energy PL emission. The former is emissions type in few millieletronvolts close to the upper part of VB or to the lower part of CB, and monoionized defects type are predominant, which results to a more energetic PL emission (cyan-blue-violet colors). Deep type emissions are further away this maximum and minimum bands with duple-ionized defect type (lower energetic emission, green-yellow-orange-red colors) [75][5][76].

The spectra deconvoluted, Figure S6, show that the PMO sample and solid solution samples have mainly emissions with deep defects type (500-700 nm)- the PMO sample has 76% emission in the green region, Figure S6a, and that by decreasing the concentration of Pb, the emission in the green region decreases, increasing the emission in the red region, Figures S6b-e. The CSMO sample as shown in the spectrum presents shallow and deep defects type with 40% emission in green and 40% emission in blue, Figure S6f. Figure 13a-c shows the emission transition states and its relation with the band gap for the PMO, Pb0.8 and Pb0.6 samples, respectively. This relationship allows us to better consider the shallow and deep levels of each spectrum of the samples [77][78]. It would be expected that only the CSMO sample has characteristics of shallow defects, $V_o^{\cdot}$ type. However, considering the diagram (Figure 13), it is possible to observe that PMO, Pb0.8 and Pb0.6 samples have defect levels below 0.8 eV characteristic of shallow defects [76][75].

Therefore, considering the types of defects on exposed surfaces for each sample (Figure 7 and S4) and their corresponding gap energy (Table S3), the emission types for each material were defined, as shown in the Figure 13. As seen in 3.3 section, the PMO morphology presents concomitant (001), (112), and (011) surfaces, being the first and second surfaces composed by defects with two oxygen vacancies $[PbO_6...2V_O^x]$, while the last one with three vacancies, $[PbO_5...3V_O^x]$. Considering that the (011) and (112) surfaces have similar E_{gap} (3.62 and 3.60 eV), and the (001) surface has $E_{gap} = 3.56$ eV, is expected that shallow defects to be related to the chemical environment of the higher gap energy surfaces, while that deep defects to be related to the chemical environment of the lower gap energy surfaces. Thus, for PMO sample as shallow defects the chemical environment will be composed by (011) surface with Pb and Mo clusters interaction ($[PbO_5.3V_O^{\cdot}]$-2$[MoO_4]$'-$[PbO_8]$'), and for the (112) surface with the chemical environment of: 2$[PbO_6.2V_O^{\cdot}]$ -2$[MoO_4]$'. While the deep defects would be related to the (001) surface with the following chemical environment: $[PbO_6.2V_O^{\cdot\cdot}]$-$[MoO_4]$"-$[PbO_8]$", Figure 13a. For the Pb0.8 sample, only the (011) surface is obtained in its morphology and thus the exposed clusters of Ca and its neighborhood with Mo and Sr clusters are the chemical environment for this surface. For this sample the defects of the shallow type are due to $[CaO_5.3V_O^{\cdot}]$-2$[MoO_4]$'-$[SrO_8]$' and similar for deep defects, ($[CaO_5.3V_O^{\cdot\cdot}]-2[MoO_4]$"-$[SrO_8]$"), Figure 13b. An interesting factor is observed for the Pb0.6 sample which has the (011) and (110) surfaces in its morphology and both have a chemical environment composed of the Ca cluster around two Mo clusters. The surface with the highest gap energy, (011), is the responsible for the emission of shallow defects ($[CaO_5.3V_O^{\cdot}]$-2$[MoO_4]$'), while the one with the lowest gap energy, (110) surface, for the emission of deep defects ($[CaO_5.3V_O^{\cdot\cdot}]-2[MoO_4]$"), Figure 13c.

3.6. Degradation process of RhB dye

The photocatalytic performance was tested via degradation of the RhB solution under UV light. A graph of (C/C_0) vs. reaction time is presented in Figure 14a, where C is the concentration of RhB solution at time t and C_0 is the initial concentration for samples. The behavior observed in the $-\ln(C/C_0)$ vs. reaction time diagram shown in Figure 14b suggests a first-order kinetic reaction. Their analysis showed that with increasing concentration of the Ca/Sr cations (and consequently the decrease in the concentration of Pb cations), a reduction in the photodegradation process of the RhB can be observed. The kinetic constant is reduced from $1 \cdot 10^{-2}$ min^{-1} to $1 \cdot 10^{-3}$ min^{-1} in passing from PMO to CSMO, respectively. The improvement in the dye molecules degradation process, using a photocatalyst, is associated with the numbers of the electron-hole pair available on the surface of the photocatalyst and its low recombination rate [49]. Thus, the PMO and the samples with higher concentrations of Pb cations (Pb0.8 and Pb0.6) presented better results in the RhB degradation. The photocatalysts electronic band structure, which is one of the responsible for the photocatalytic efficiency, can be tuned changing the specific exposed surfaces [79], as observed for calculated values of band gap energy for the PMO and $Pb_{1-2x}Ca_xSr_xMoO_4$ surfaces, Table S3. In addition, a comparison of DOS for PMO and CSMO surfaces is presented in Figures S7 and S8, showing a similar split-off feature at the VB and the CB compared to the bulk of pure and doped systems, where the transfer of electrons is produced to generate the electron/hole pairs.

Table S4 shows the calculated values of the Mulliken population per atom and constitutive cluster for PMO and CSMO bulk, as well as the Mulliken population per undercoordinated cluster of surfaces. This analysis is a helpful tool that allows clarification of the nature of the electron-hole localization in the undercoordinated

clusters at the exposed surfaces. An analysis of the results shows that for both PMO and CSMO bulk structures there is an accumulation of electrons at the [Pb/Ca/SrO$_8$] clusters and there is an electron depletion (positive charge accumulation) at the [MoO$_4$] cluster, thereby creating a difference in potential which is able to form a local electric field. In PMO the potential between [PbO$_8$] and [MoO$_4$] clusters are compensated, and the same occurs between the [Ca/SrO$_8$] and [MoO$_4$] clusters in CSMO. However, a local electric field is generated and also tends to vary on surfaces according to the number of O atom vacancies in the exposed surface clusters [80]. These differences in charge in the different clusters of the surface have an influence on the transfer of the photogenerated electron-hole.

For example, the (011), (110), (100) and (111) surfaces have higher values of D_b, compared to (001) and (112), and the presence of three oxygen vacancies [PbO$_5$…3V$_o^x$], which generate higher charge differences between [Pb/Ca/SrO$_5$] and [MoO$_4$] clusters. Accordingly, it is observed that not only the undercoordinated cations of the exposed clusters play a decisive role in the surfaces that constitute the morphology, but they are also involved in the structural and electronic distortion of the clusters (see Table S1). The information from the FE-SEM image reveals that the presence of nanoparticles with an octahedral morphology is controlled mainly by (001), (011) and (112) exposed surfaces. As the concentration of Pb in the samples decreases, the surface (001) becomes less predominant and the surface (110) appears in the sample Pb0.6, the most photoactive. It was observed that between the PMO and Pb0.6 samples the E$_{gap}$ of the surfaces increases, Table S3, and the potential difference becomes greater for the [CaO$_{8-y}$.yV_O^x] and [MoO$_4$] clusters on the surface (110) as the content of Pb decreases, Table S4. This fact can enhance the migration of photoinduced electrons for the surface, suppressing the recombination of charge carriers, and improving the photocatalytic activity.

Moreover, the migrated electrons can be trapped by the oxygen molecules, O_2, adsorbed on the surface to generate $O_2^{.-}$ radicals, while the holes on the surface react with water molecules to yield $OH^.$ and $H^.$ radicals. Furthermore, these photogenerated reactive oxygen species induce the degradation of RhB. Consequently, the undercoordinated and complete clusters at the surfaces, $[CaO_x]/[SrO_x]/[PbO_x]$ and distorted $[MoO_4]_d$ are the active sites capable of reacting with H_2O and O_2, respectively, and can be considered the reservoirs of holes and electrons, respectively, that constitute the active sites in the photocatalytic activity.

5. CONCLUSIONS

This study reports the successful preparation of PMO and $Pb_{1-2x}Ca_xSr_xMoO_4$ (x= 0.1, 0.2, 0.3, 0.4 and 0.5) solid solutions in the whole compositional range. Their structural, electronic, and vibrational properties, as well as the morphologies and the photocatalytic activity in the photodegradation process of RhB dye have been investigated. The samples synthesized with higher concentrations of Pb cations presented better results in RhB degradation. The photocatalysts' electronic band structure, which has an influence on photocatalysts, can be tuned using the specific exposed surfaces, and this has a significant impact on the redox abilities of photoinduced carriers. First-principles calculations were performed to obtain the energy surface values for the PMO and solid solution surfaces, based on the Wulff construction, in order to rationalize the crystal morphologies observed in the experimental FE-SEM images.

The simulations revealed that there are two important factors that must be considered when investigating the surface electronic properties of the as-synthesized samples. The first factor is that the (011) and (110) surfaces appear in the experimental FE-SEM images which show enhanced photocatalytic activity. The second involves the specific local coordination of the Pb/Ca/Sr and Mo cations in the exposed surface, i.e., the Pb/Ca/Sr

and Mo clusters. In particular, we found that the stability of the surfaces and their electronic properties are correlated with the presence of incomplete $[CaO_x]/[SrO_x]/[PbO_x]$ and distorted $[MoO_4]$ clusters as the reservoirs of holes and electrons, respectively, which act as the active sites in the photocatalytic activity. These subtle differences between the (011), (110) and (112) surfaces illustrate the influence of surface type on reactivity. Controlling for the combination of surface types in the morphology thus provides an extremely sensitive tuning mechanism for the location of active sites. The PL emission spectra of the samples showed predominant emission in the green-orange region, with predominantly shallow type defects for the most photoactive samples. Overall, the current study opens the door to further uses of solid solutions based on PMO with tunable properties for various applications. The reported synthetic approach is believed to have potential utility for obtaining other solid solutions, while the results described here provide new insights on the geometry, electronic structure, morphology evolution, and structure–property relationship of $AMoO_4$-type compounds. These findings show that by directing the crystal morphology it is possible to control and understand its properties, such as optical and photocatalytic properties. Exploration of semiconductor surface effects may lead to the fabrication of more efficient photocatalysts.

ACKNOWLEDGMENTS

REFERENCES

[1] Valeria M. Longo, Laecio S. Cavalcante, Elaine C. Paris, Julio C. Sczancoski, Paulo S. Pizani, Maximo Siu Li, Juan Andres, Elson Longo, Jose A. Varela, "Hierarchical Assembly of $CaMoO_4$ Nano-Octahedrons and Their Photoluminescence Properties," *J. Phys. Chem. C*, vol. 115, no. 13, pp. 5207–5219, 2011.

[2] R. Grissa, H. Martinez, V. Pelé, S. Cotte, B. Pecquenard, and F. Le Cras, "An X-ray photoelectron spectroscopy study of the electrochemical behaviour of iron molybdate thin films in lithium and sodium cells," *J. Power Sources*, vol. 342, pp. 796–807, 2017.

[3] J. Zhang, T. Zhao, L. Zou, and S. Gan, "Ultrasound-assisted precipitation synthesis of $PbMoO_4$ and $PbMoO_4$:Eu^{3+} nanocrystals and photoluminescence properties," *J. Photochem. Photobiol. A Chem.*, vol. 314, pp. 35–41, Jan. 2016.

[4] S. S. Hosseinpour-Mashkani, S. S. Hosseinpour-Mashkani, and A. Sobhani-Nasab, "Synthesis and characterization of rod-like $CaMoO_4$ nanostructure via free surfactant sonochemical route and its photocatalytic application," *J. Mater. Sci. Mater. Electron.*, vol. 27, no. 5, pp. 4351–4355, 2016.

[5] M.R.D.Bomio, L.S.Cavalcante, M.A.P.Almeida, R.L.Tranquilin, N.C.Batista, P.S.Pizani, M.Siu Lie, J.Andres, E.Longo, "Structural refinement, growth mechanism, infrared/Raman spectroscopies and photoluminescence properties of $PbMoO_4$ crystals," *Polyhedron*, vol. 50, no. 1, pp. 532–545, 2013.

[6] T.Skibiński, S.M.Kaczmarek, G.Leniec, T.Tsuboi, Y.Nakai, M.Berkowski, Z.Kowalski, W.Huang, "Magnetic and optical properties of Co-doped $PbMoO_4$ single crystals," *J. Cryst. Growth*, vol. 401, pp. 802–806, 2014.

[7]   G.M. Gurgel, L.X. Lovisa , L.M. Pereira, F.V. Motta, M.S. Li, E. Longo, C.A. Paskocimas, M.R.D. Bomio, "Photoluminescence properties of (Eu, Tb, Tm) co-doped PbMoO4 obtained by sonochemical synthesis," *J. Alloys Compd.*, vol. 700, pp. 130–137, Apr. 2017.

[8]   Y. I. Song and S. S. Hong, "Synthesis of $Pb_xCr_{1-x}MoO_4$ oxides using microwave process and their photocatalytic activity under visible light irradiation," *Res. Chem. Intermed.*, vol. 42, no. 1, pp. 367–377, 2016.

[9]   S. Obregón, D. B. Hernández-Uresti, A. Vázquez, and D. Sánchez-Martínez, "Electrophoretic deposition of $PbMoO_4$ nanoparticles for photocatalytic degradation of tetracycline," *Appl. Surf. Sci.*, vol. 457, no. May, pp. 501–507, 2018.

[10]   D. B. Hernández-Uresti, A. Martínez-De La Cruz, and J. A. Aguilar-Garib, "Photocatalytic activity of $PbMoO_4$ molybdate synthesized by microwave method," *Catal. Today*, vol. 212, no. 3, pp. 70–74, 2013.

[11]   J.V.B. Moura, T.S. Freitas, A.R.P. Silva, A.T.L. Santos, J.H. da Silva, R.P. Cruz, R.L.S. Pereira, P.T.C. Freire, C. Luz-Lima, G.S. Pinheiro, H.D.M. Coutinho, "Synthesis, characterizations, and antibacterial properties of $PbMoO_4$ nanocrystals," *Arab. J. Chem.*, vol. 11, no. 6, pp. 739–746, 2018.

[12]   C. Pupp, R. Yamdagni, and R. F. Porter, "Mass spectrometric study of the evaporation of $BaMoO_4$ and $BaWO_4$," *J. Inorg. Nucl. Chem.*, vol. 31, no. 7, pp. 2021–2029, Jul. 1969.

[13]   C. Cui, J. Bi, C. Wu, S. Zhang, and D. Gao, "Novel electrochemical technique: Grain control in preparation of polycrystalline $BaMoO_4$ film," *Mater. Res. Bull.*, vol. 43, no. 5, pp. 1160–1163, May 2008.

[14] C.-T. Xia, V. M. Fuenzalida, and R. A. Zará, "Electrochemical preparation of crystallized $Ba_{1-x}Sr_xMoO_4$ solid-solution films at room-temperature," *J. Alloys Compd.*, vol. 316, pp. 250–255, 2001.

[15] A. P. de Azevedo Marques, Valeria M. Longo, Dulce M.A. de Melo, Paulo S. Pizani, Edson R. Leite, Jose A. Varela, Elson Longo, "Shape controlled synthesis of $CaMoO_4$ thin films and their photoluminescence property," *J. Solid State Chem.*, vol. 181, no. 5, pp. 1249–1257, 2008.

[16] Y. Mi, Z. Huang, F. Hu, and X. Li, "Room temperature reverse-microemulsion synthesis and photoluminescence properties of uniform $BaMoO_4$ submicro-octahedra," *Mater. Lett.*, vol. 63, no. 9–10, pp. 742–744, Apr. 2009.

[17] J. H. Ryu, J.-W. Yoon, C. S. Lim, and K. B. Shim, "Microwave-assisted synthesis of barium molybdate by a citrate complex method and oriented aggregation," *Mater. Res. Bull.*, vol. 40, no. 9, pp. 1468–1476, Sep. 2005.

[18] C. Zhang, E. Shen, E. Wang, Z. Kang, L. Gao, C. Hu, L. Xu, "One-step solvothermal synthesis of high ordered $BaWO_4$ and $BaMoO_4$ nanostructures," *Mater. Chem. Phys.*, vol. 96, no. 2–3, pp. 240–243, Apr. 2006.

[19] Z. Luo, H. Li, H. Shu, K. Wang, J. Xia, and Y. Yan, "Self-assembly of $BaMoO_4$ single-crystalline nanosheets into microspheres," *Mater. Chem. Phys.*, vol. 110, no. 1, pp. 17–20, Jul. 2008.

[20] S. K. Aditha, A. D. Kurdekar, L. A. A. Chunduri, S. Patnaik, and V. Kamisetti, "Aqueous based reflux method for green synthesis of nanostructures: Application in CZTS synthesis," *MethodsX*, vol. 3, pp. 35–42, Jan. 2016.

[21] V. Sabaghi, F. Davar, and Z. Fereshteh, "ZnS nanoparticles prepared via simple reflux and hydrothermal method: Optical and photocatalytic properties," *Ceram.*

Int., vol. 44, no. 7, pp. 7545–7556, 2018.

[22] P. D. Cozzoli, A. Kornowski, and H. Weller, "Low-Temperature Synthesis of Soluble and Processable Organic-Capped Anatase TiO_2 Nanorods," *J. Am. Chem. Soc.*, vol. 125, no. 47, pp. 14539–14548, 2003.

[23] Y. Sun, B. Gates, B. Mayers, and Y. Xia, "Crystalline Silver Nanowires by Soft Solution Processing," *Nano Lett.*, vol. 2, no. 2, pp. 165–168, 2002.

[24] Marisa C. Oliveira, Juan Andrésa, Lourdes Graciac, M. Suzane M.P. de Oliveira, Jose Manuel R. Mercury, Elson Longo, Içamira C. Nogueira, "Geometry, electronic structure, morphology, and photoluminescence emissions of $BaW_{1-x}Mo_xO_4$(x = 0, 0.25, 0.50, 0.75, and 1) solid solutions: Theory and experiment in concert," *Appl. Surf. Sci.*, vol. 463, no. May 2018, pp. 907–917, 2019.

[25] S. Vidya, S. Solomon, and J. K. Thomas, "Structral, Optical and Dielectric Characterization of Nanocrystalline $AMo_{0.5}W_{0.5}O_4$ (where A=Ba, Sr and Ca) Prepared by Single Step Modified Combustion Technique," *Mater. Today Proc.*, vol. 2, no. 3, pp. 904–908, 2015.

[26] I. C. Nogueira, L. S. Cavalcante, P. F. S. Pereira, M. M. de Jesus, J. M. Rivas Mercury, N. C. Batista, M. S. Li and E. Longo, "Rietveld refinement, morphology and optical properties of $(Ba_{1-x}Sr_x)MoO_4$ crystals," *J. Appl. Crystallogr.*, vol. 46, no. 5, pp. 1434–1446, Oct. 2013.

[27] V. D. Zhuravlev, O. G. Reznitskikh, Y. A. Velikodnyi, T. A. Patrusheva, and O. V. Sivtsova, "Analysis of solid solutions stability in scheelite-type molybdates and tungstates," *J. Solid State Chem.*, vol. 184, no. 10, pp. 2785–2789, Oct. 2011.

[28] S. P. Culver, M. J. Greaney, A. Tinoco, and R. L. Brutchey, "Lowerature synthesis of homogeneous solid solutions of scheelite-structured $Ca_{1-x}Sr_xWO_4$ and Sr_{1-}

$_x$Ba$_x$WO$_4$ nanocrystals," *Dalt. Trans.*, vol. 44, no. 33, pp. 15042–15048, 2015.

[29] Y. Wang, C. Wu, L. Geng, and S. Chen, "Unexpected formation of scheelite-structured Ca$_{1-x}$Cd$_x$WO$_4$ ($0 \leq x \leq 1$) continuous solid solutions with tunable photoluminescent and electronic properties," *Phys. Chem. Chem. Phys.*, vol. 19, no. 34, pp. 23204–23212, 2017.

[30] A. Hallaoui, A. Taoufyq, M. Arab, B. Bakiz, A. Benlhachemi, L. Bazzi, J-C. Valmalette, S. Villaina, F. Guinnetona, J-R. Gavarri., "Structural, vibrational and photoluminescence properties of Sr$_{(1-x)}$Pb$_x$MoO$_4$ solid solution synthesized by solid state reaction," *Mater. Res. Bull.*, vol. 79, pp. 121–132, 2016.

[31] Paula F. S. Pereira, Clayane C. Santos, Amanda F. Gouveia, Mateus M. Ferrer, Ivo M. Pinatti, Gleice Botelho, Julio R. Sambrano, Ieda L. V. Rosa, Juan Andrés, Elson Longo, "α-Ag$_{2-2x}$Zn$_x$WO$_4$ ($0 \leq \times \leq 0.25$) Solid Solutions: Structure, Morphology, and Optical Properties," *Inorg. Chem.*, vol. 56, no. 13, pp. 7360–7372, 2017.

[32] W. da Silva Pereira, Mateus M. Ferrer, Gleice Botelho, Lourdes Gracia, Içamira C. Nogueira, Ivo M. Pinatti, Ieda L. Viana Rosa, Felipe de A. La Porta, Juan Andres, Elson Longo, "Effects of chemical substitution on the structural and optical properties of α-Ag$_{2-2x}$Ni$_x$WO$_4$ ($0 \leq x \leq 0.08$) solid solutions," *Phys. Chem. Chem. Phys.*, vol. 18, no. 31, pp. 21966–21975, 2016.

[33] R. Dovesi, A. Erba, R. Orlando, Claudio M. Zicovich-Wilson, Bartolomeo Civalleri, Lorenzo Maschio, Michel Rérat, Silvia Casassa, Jacopo Baima, Simone Salustro, Bernard Kirtman, "Quantum-mechanical condensed matter simulations with CRYSTAL," *Wiley Interdiscip. Rev. Comput. Mol. Sci.*, vol. 8, no. 4, pp. 1–36, 2018.

[34] Z. Gao, W. Sun, Y. Hu, X. Liu, "Anisotropic surface broken bond properties and

wettability of calcite and fluorite crystals," *Trans. Nonferrous Met. Soc. China*, vol. 22, no. 5, pp. 1203–1208, 2012.

[35] Z. Gao, C. Li, W. Sun, and Y. Hu, "Anisotropic surface properties of calcite: A consideration of surface broken bonds," *Colloids Surfaces A Physicochem. Eng. Asp.*, vol. 520, pp. 53–61, May 2017.

[36] M. M. Ferrer, A. F. Gouveia, L. Gracia, E. Longo, and J. Andrés, "A 3D platform for the morphology modulation of materials: First principles calculations on the thermodynamic stability and surface structure of metal oxides: Co_3O_4, α-Fe_2O_3, and In_2O_3," *Model. Simul. Mater. Sci. Eng.*, vol. 24, no. 2, 2016.

[37] G. Wulff, "XXV. Zur Frage der Geschwindigkeit des Wachsthums und der Auflösung der Krystallflächen," *Zeitschrift für Krist. - Cryst. Mater.*, vol. 34, no. 1–6, 2014.

[38] J. Andrés, L. Gracia, A. F. Gouveia, M. M. Ferrer, and E. Longo, "Effects of surface stability on the morphological transformation of metals and metal oxides as investigated by first-principles calculations.," *Nanotechnology*, vol. 26, no. 40, p. 405703, 2015.

[39] M. R. D. Bomio, R. L. Tranquilin, F. V. Motta, C. A. Paskocimas, R. M. Nascimento, L. Gracia, J. Andres, E. Longo, "Toward understanding the photocatalytic activity of $PbMoO_4$ powders with predominant (111), (100), (011), and (110) facets. A combined experimental and theoretical study," *J. Phys. Chem. C*, vol. 117, no. 41, pp. 21382–21395, 2013.

[40] Valeria M. Longo, Laecio S. Cavalcante, Elaine C. Paris, Julio C. Sczancoski, Paulo S. Pizani, Maximo Siu Li, Juan Andres, Elson Longo, Jose A. Varela, "Hierarchical Assembly of $CaMoO_4$ Nano-Octahedrons and Their

Photoluminescence Properties," *J. Phys. Chem. C*, vol. 115, no. 13, pp. 5207–5219, Apr. 2011.

[41] G. Botelho, I. C. Nogueira, E. Moraes, and E. Longo, "Study of structural and optical properties of $CaMoO_4$ nanoparticles synthesized by the microwave-assisted solvothermal method," *Mater. Chem. Phys.*, vol. 183, pp. 110–120, 2016.

[42] Maria T. Fabbro, Carla Saliby, Larissa R. Rios, Felipe A. La Porta, Lourdes Gracia, Máximo S. Li, Juan Andrés, Luís P. S. Santos, Elson Longo, "Identifying and rationalizing the morphological, structural, and optical properties of β-Ag_2MoO_4 microcrystals, and the formation process of Ag nanoparticles on their surfaces: Combining experimental data and first-principles calculations," *Sci. Technol. Adv. Mater.*, vol. 16, no. 6, p. 65002, 2015.

[43] Marisa C. Oliveira, Lourdes Gracia, Içamira C. Nogueira, Maria Fernanda C. Gurgel, Jose Manuel R. Mercury, Elson Longo, Juan Andres, "On the morphology of $BaMoO_4$ crystals: A theoretical and experimental approach," *Cryst. Res. Technol.*, vol. 51, no. 10, pp. 634–644, 2016.

[44] Marisa C. Oliveira, Lourdes Gracia, Içamira C. Nogueira, Maria Fernanda C. Gurgel, Jose Manuel R. Mercury, Elson Longo, Juan Andres, "Synthesis and morphological transformation of $BaWO_4$ crystals: Experimental and theoretical insights," *Ceram. Int.*, vol. 42, no. 9, pp. 10913–10921, 2016.

[45] Gabriela S. Silva, Lourdes Gracia, Maria T. Fabbro, Luis P. Serejo dos Santos, Hector Beltrán-Mir, Eloisa Cordoncillo, Elson Longo, Juan Andrés, "Theoretical and Experimental Insight on Ag_2CrO_4 Microcrystals: Synthesis, Characterization, and Photoluminescence Properties," *Inorg. Chem.*, vol. 55, no. 17, pp. 8961–8970, 2016.

[46]   A. F. Gouveia, M. M. Ferrer, J. R. Sambrano, J. Andrés, and E. Longo, "Modeling the atomic-scale structure, stability, and morphological transformations in the tetragonal phase of LaVO$_4$," *Chem. Phys. Lett.*, vol. 660, pp. 87–92, 2016.

[47]   T. T. Basiev, A. A. Sobol, Y. K. Voronko, and P. G. Zverev, "Spontaneous Raman spectroscopy of tungstate and molybdate crystals for Raman lasers," *Opt. Mater. (Amst).*, vol. 15, no. 3, pp. 205–216, 2000.

[48]   K. T. Lim, G. D. Lee, S.-S. Hong, W. Y. Jung, and M. S. Lee, " Synthesis of PbMoO$_4$ Nanoparticles Using a Facile Surfactant-Assisted Microwave Process and Their Photocatalytic Activity ," *J. Nanosci. Nanotechnol.*, vol. 17, no. 4, pp. 2751–2755, 2017.

[49]   L. Zhang, D. Bai, M. Zhou, and C. Pan, "Surfactant-free hydrothermal synthesis, growth mechanism and photocatalytic properties of PbMoO$_4$ polyhedron microcrystals," *J. Saudi Chem. Soc.*, vol. 21, pp. S275–S282, Jan. 2017.

[50]   T. Thongtem, S. Kungwankunakorn, B. Kuntalue, A. Phuruangrat, and S. Thongtem, "Luminescence and absorbance of highly crystalline CaMoO$_4$, SrMoO$_4$, CaWO$_4$ and SrWO$_4$ nanoparticles synthesized by co-precipitation method at room temperature," *J. Alloys Compd.*, vol. 506, no. 1, pp. 475–481, 2010.

[51]   V.D. Araújo, R.L. Tranquilin, F.V. Motta, C.A. Paskocimas, M.I.B. Bernardi, L.S. Cavalcante, J. Andres, E. Longo, M.R.D. Bomio, "Effect of polyvinyl alcohol on the shape, photoluminescence and photocatalytic properties of PbMoO$_4$ microcrystals," *Mater. Sci. Semicond. Process.*, vol. 26, pp. 425–430, Oct. 2014.

[52]   F. A. Kröger and H. J. Vink, "Relations between the Concentrations of Imperfections in Crystalline Solids," *Solid State Phys.*, vol. 3, pp. 307–435, Jan.

1956.

[53]   F.K.F. Oliveira, M.C. Oliveira, L. Gracia, R.L. Tranquilin, C.A. Paskocimas, F.V. Motta, E. Longo, J. Andres, M.R.D. Bomio, "Experimental and theoretical study to explain the morphology of $CaMoO_4$ crystals," *J. Phys. Chem. Solids*, vol. 114, no. June 2017, pp. 141–152, 2018.

[54]   L. S. Cavalcante, J. C. Sczancoski, R. L. Tranquilin, J. A. Varela, E. Longo, and M. O. Orlandi, "Growth mechanism of octahedron-like $BaMoO_4$ microcrystals processed in microwave-hydrothermal: Experimental observations and computational modeling," *Particuology*, vol. 7, no. 5, pp. 353–362, Oct. 2009.

[55]   L. Tolvaj, K. Mitsui, and D. Varga, "Validity limits of Kubelka-Munk theory for DRIFT spectra of photodegraded solid wood," *Wood Sci. Technol.*, vol. 45, no. 1, pp. 135–146, 2011.

[56]   D. L. Wood, J. Tauc, "Weak Absorption Tails in Amorphous Semiconductors," *Phys. Rev. B*, vol. 5, no. 8, pp. 3144–3151, 1972.

[57]   V. S. Marques, L. S. Cavalcante, J. C. Sczancoski, A. F. P. Alcantara, M. O. Orlandi, E. Moraes, E. Longo, J. A. Varela, M. Siu Li, M. R. M. C. Santos, "Effect of different solvent ratios (water/ethylene glycol) on the growth process of $CaMoO_4$ crystals and their optical properties," *Cryst. Growth Des.*, vol. 10, no. 11, pp. 4752–4768, 2010.

[58]   Valeria M. Longo, Alberthmeiry T. de Figueiredo, Adaci B. Campos, Jose W. M. Espinosa, Antonio C. Hernandes, C. A. Taft, Julio R. Sambrano, Jose A. Varela, Elson Longo, "Different origins of green-light photoluminescence emission in structurally ordered and disordered powders of calcium molybdate," *J. Phys.*

Chem. A, vol. 112, no. 38, pp. 8920–8928, 2008.

[59]   G. Botelho, I. C. Nogueira, E. Moraes, and E. Longo, "Study of structural and optical properties of $CaMoO_4$ nanoparticles synthesized by the microwave-assisted solvothermal method," *Mater. Chem. Phys.*, vol. 183, pp. 110–120, Nov. 2016.

[60]   Maria Fernanda C. Abreu Fabiana V.Motta Renata C.Lima Maximo S.Li Elson Longo Ana Paula de A.Marques, "Effect of process parameters on photophysical properties and barium molybdate phosphors characteristics," *Ceram. Int.*, vol. 40, no. 5, pp. 6719–6729, Jun. 2014.

[61]   A.A.G. Santiago, C.R.R. Almeida, R.L. Tranquilin, R.M. Nascimento, C.A. Paskocimas, E. Longo, F.V. Motta, M.R.D. Bomio, "Photoluminescent properties of the $Ba_{1-x}Zn_xMoO_4$ heterostructure obtained by ultrasonic spray pyrolysis," *Ceram. Int.*, vol. 44, no. 4, pp. 3775–3786, 2018.

[62]   R. Vali, "Electronic properties and phonon spectra of $SrMoO_4$," *Comput. Mater. Sci.*, vol. 50, no. 9, pp. 2683–2687, 2011.

[63]   D. A. Spassky, N. S. Kozlova, V. Nagirnyi, A. E. Savon, Y. A. Hizhnyi, and S. G. Nedilko, "Excitation energy transfer to luminescence centers in $M^{II}MoO_4$ (M^{II} = Ca, Sr, Zn, Pb) and Li_2MoO_4," *J. Lumin.*, vol. 186, pp. 229–237, 2017.

[64]   Y. Zhang, N. A. W. Holzwarth, and R. T. Williams, "Electronic band structures of the scheelite materials $CaMoO_4$, $CaWO_4$, $PbMoO_4$, and $PbWO_4$," vol. 57, no. 20, pp. 738–750, 1998.

[65]   H. Kadowaki, N. Saito, H. Nishiyama, H. Kobayashi, Y. Shimodaira, and Y. Inoue, " Overall Splitting of Water by RuO_2 -Loaded $PbWO_4$ Photocatalyst with d^{10} $s^{2-}d^0$ Configuration ," *J. Phys. Chem. C*, vol. 111, no. 1, pp. 439–444, 2006.

[66] A. Hofstaetter, R. Oeder, A. Scharmann, and D. Sciiwabe, "Paramagnetic Resonance and Thermoluminescence of the PbWO₄/PbMoO₄ Mixed Crystal System," vol. 375, 1978.

[67] J. C. Sczancoski, M. D. R. Bomio, L. S. Cavalcante, M. R. Joya, P. S. Pizani, J. A. Varela, E. Longo, M. Siu Li, J. A. Andrés, "Morphology and blue photoluminescence emission of PbMoO₄ processed in conventional hydrothermal," *J. Phys. Chem. C*, vol. 113, no. 14, pp. 5812–5822, 2009.

[68] J. Bi, L. Wu, Y. Zhang, Z. Li, J. Li, and X. Fu, "Solvothermal preparation, electronic structure and properties of PbMoO₄ and SrMoO₄," *Appl. Catal. B Environ.*, vol. 91, no. 1–2, pp. 135–143, 2009.

[69] Dmitry A. Spassky, Sergey N. Ivanov, Vitaly N. Kolobanov, Vitaly V. Mikhailin, Vladimir N. Zemskov, Boris I. Zadneprovski, Leonid I. Potkin, "Optical and luminescent properties of the lead and barium molybdates," *Radiat. Meas.*, vol. 38, no. 4–6, pp. 607–610, Aug. 2004

[70] J. W. Yoon, J. H. Ryu, and K. B. Shim, "Photoluminescence in nanocrystalline MMoO₄ (M = Ca, Ba) synthesized by a polymerized complex method," *Mater. Sci. Eng. B Solid-State Mater. Adv. Technol.*, vol. 127, no. 2–3, pp. 154–158, 2006.

[71] W. S. Wang, L. Zhen, C. Y. Xu, and W. Z. Shao, "Room temperature synthesis, growth mechanism, photocatalytic and photoluminescence properties of cadmium molybdate core-shell microspheres," *Cryst. Growth Des.*, vol. 9, no. 3, pp. 1558–1568, 2009.

[72] X. Pan, M. Q. Yang, X. Fu, N. Zhang, and Y. J. Xu, "Defective TiO₂ with oxygen vacancies: Synthesis, properties and photocatalytic applications," *Nanoscale*, vol. 5, no. 9, pp. 3601–3614, 2013.

[73] Rafael A.C. Amoresia, Vinícius Teodoro, Guilhermina F. Teixeira, Maximo S. Li, Alexandre Z. Simões, Leinig A. Perazolli, Elson Longo,Maria A. Zaghete, "Journal of the European Ceramic Society Electrosteric colloidal stabilization for obtaining $SrTiO_3/TiO_2$ heterojunction : Microstructural evolution in the interface and photonics properties," vol. 38, no. August 2017, pp. 1621–1631, 2018.

[74] A. Arenas-hernandez, C. Zúñiga-islas, and A. Torres-jacome, "Self-organized and self-assembled TiO_2 nanosheets and nanobowls on TiO_2 nanocavities by electrochemical anodization and their properties," 2020 Nano Express 1 010054.

[75] V. M. Longo, A. T. de Figueiredo, S. de Lázaro, M. F. Gurgel, M. G. S. Costa, C. O. Paiva-Santos, J. A. Varela, E. Longo, V. R. Mastelaro, F. S. de Vicente, A. C. Hernandes, R. W. A. Franco, "Structural conditions that leads to photoluminescence emission in $SrTiO_3$: An experimental and theoretical approach," *J. Appl. Phys.*, vol. 104, no. 2, pp. 1–11, 2008.

[76] E. Silva Junior, F. A. La Porta, M. S. Liu, J. Andrés, J. A. Varela, and E. Longo, "A relationship between structural and electronic order-disorder effects and optical properties in crystalline TiO_2 nanomaterials," *Dalt. Trans.*, vol. 44, no. 7, pp. 3159–3175, 2015.

[77] Ning Zhang, Chen Chen, Zongwei Mei, Xiaohe Liu, Xiaolei Qu, Yunxiang Li, Siqi Li, Weihong Qi, Yuanjian Zhang, Jinhua Ye, Vellaisamy A. L. Roy, Renzhi Ma, "Monoclinic Tungsten Oxide with {100} Facet Orientation and Tuned Electronic Band Structure for Enhanced Photocatalytic Oxidations," *ACS Appl. Mater. Interfaces*, vol. 8, no. 16, pp. 10367–10374, 2016.

[78] R. A. Roca, J. C. Sczancoski, I. C. Nogueira, M. T. Fabbro, H. C. Alves, L. Gracia, L. P. S. Santos, C. P. de Sousa, J. Andrés, G. E. Luz Jr., E. LongoL. S. Cavalcante,

"Facet-dependent photocatalytic and antibacterial properties of α-Ag$_2$WO$_4$ crystals: combining experimental data and theoretical insights," *Catal. Sci. Technol.*, vol. 5, no. 8, pp. 4091–4107, 2015.

[79]   H. Chen and Y. Xu, "Photoactivity and stability of Ag$_2$WO$_4$ for organic degradation inaqueous suspensions," *Appl. Surf. Sci.*, vol. 319, no. 1, pp. 319–323, 2014.

[80]   Rafael A. C. Amoresi, Regiane C. Oliveira, Naiara L. Marana, Priscila B. de Almeida, Paloma S. Prata, Maria A. Zaghete, Elson Longo, Julio R. Sambrano, and Alexandre Z. Simões, "CeO$_2$ Nanoparticle Morphologies and Their Corresponding Crystalline Planes for the Photocatalytic Degradation of Organic Pollutants," 2019.

Figures
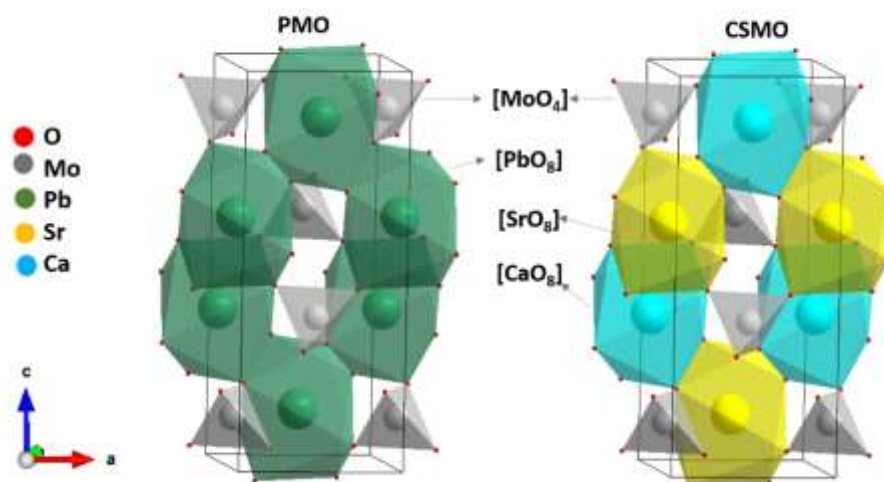
Figure 1. Unit cell of the PbMoO$_4$ and CaSrMoO$_4$. The [MoO$_4$], [PbO$_8$], [SrO$_8$] and [CaO$_8$] clusters, i.e., local coordination of Mo, Pb, Sr and Ca cations, respectively, as building blocks of the samples, are depicted for clarity purposes.
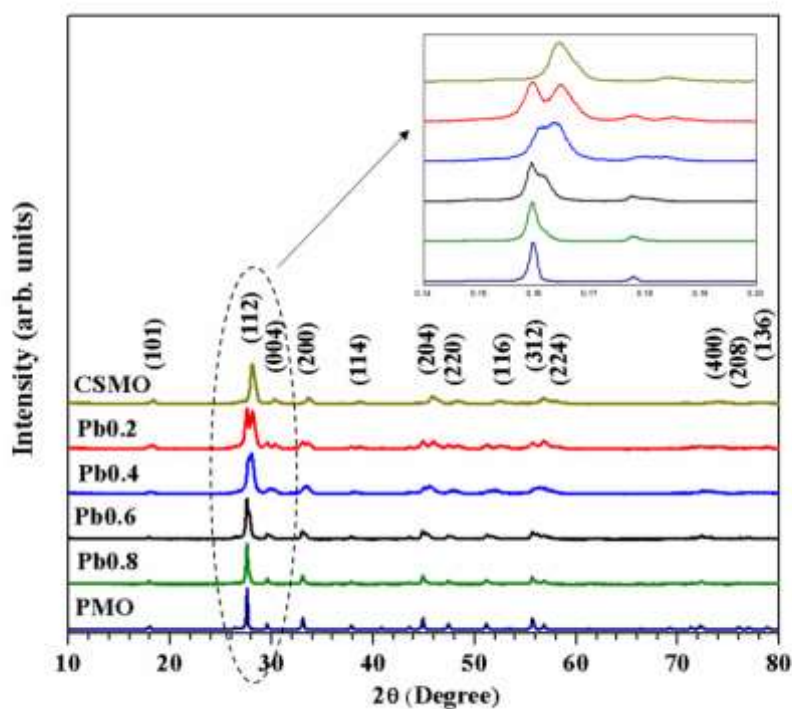
Figure 2. XRD patterns of solid solutions Pb$_{1-2x}$Ca$_x$Sr$_x$MoO$_4$. PMO (x=0), Pb0.8 (x=0.1), Pb0.6 (x=0.2), Pb0.4 (x=0.3), Pb0.2 (x=0.4), CSMO (x=0.5).
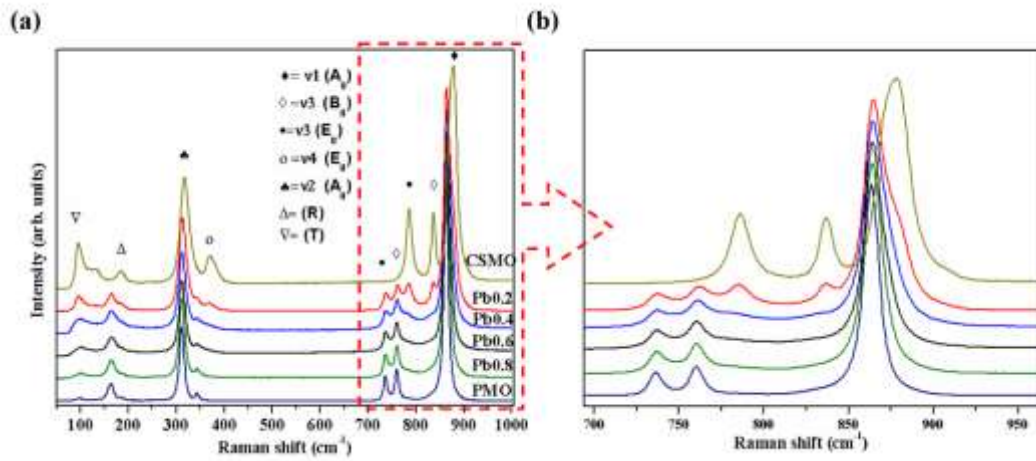
Figure 3. Micro Raman spectra in the range from 100 to 1000 cm^{-1} of (a) $Pb_{1-2x}Ca_xSr_xMoO_4$ and (b) (zoom) range from 700 to 950 cm^{-1}.
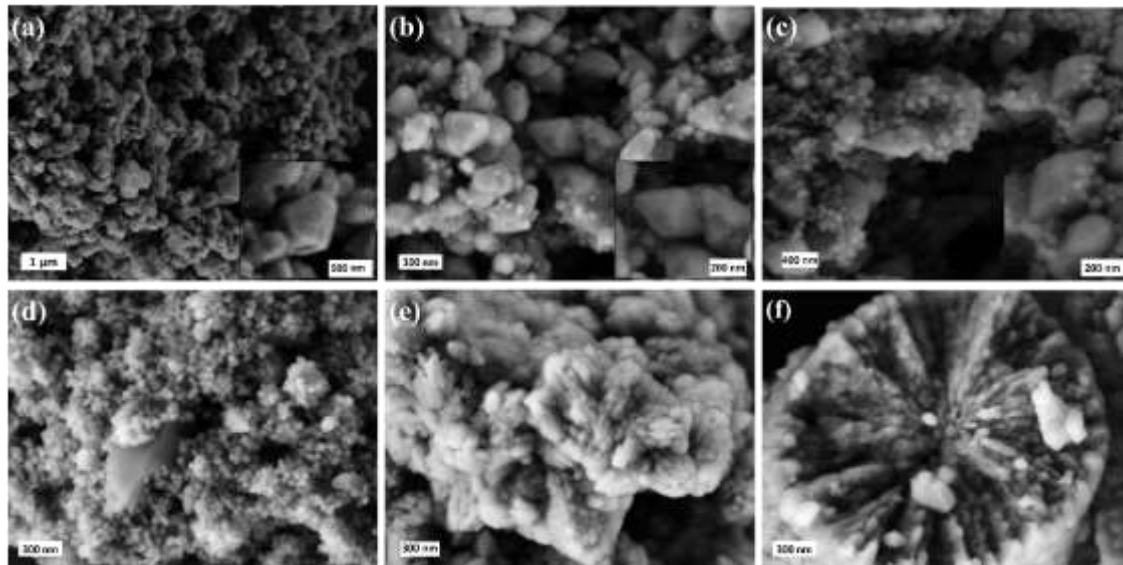
Figure 4. FE-SEM images of the samples and magnifications of the characteristic morphology of the samples (inset). (a) PMO (b) Pb0.8, (c) Pb0.6, (d) Pb0.4, (e) Pb0.2, (f) CSMO.
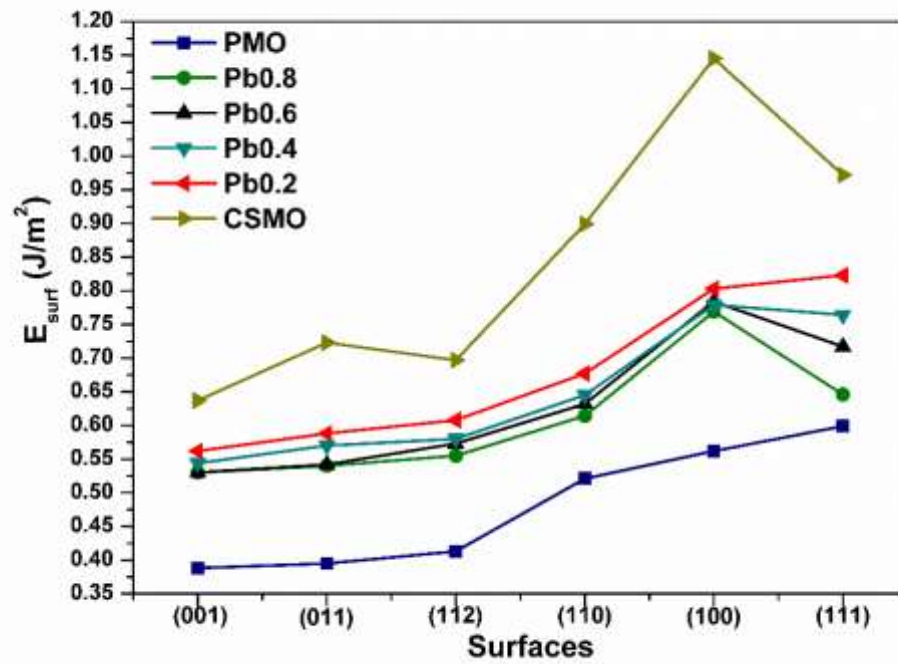
Figure 5. Calculated values of E_{surf} for the different surfaces of PMO and $Pb_{1-2x}Ca_xSr_xMoO_4$ solid solutions.
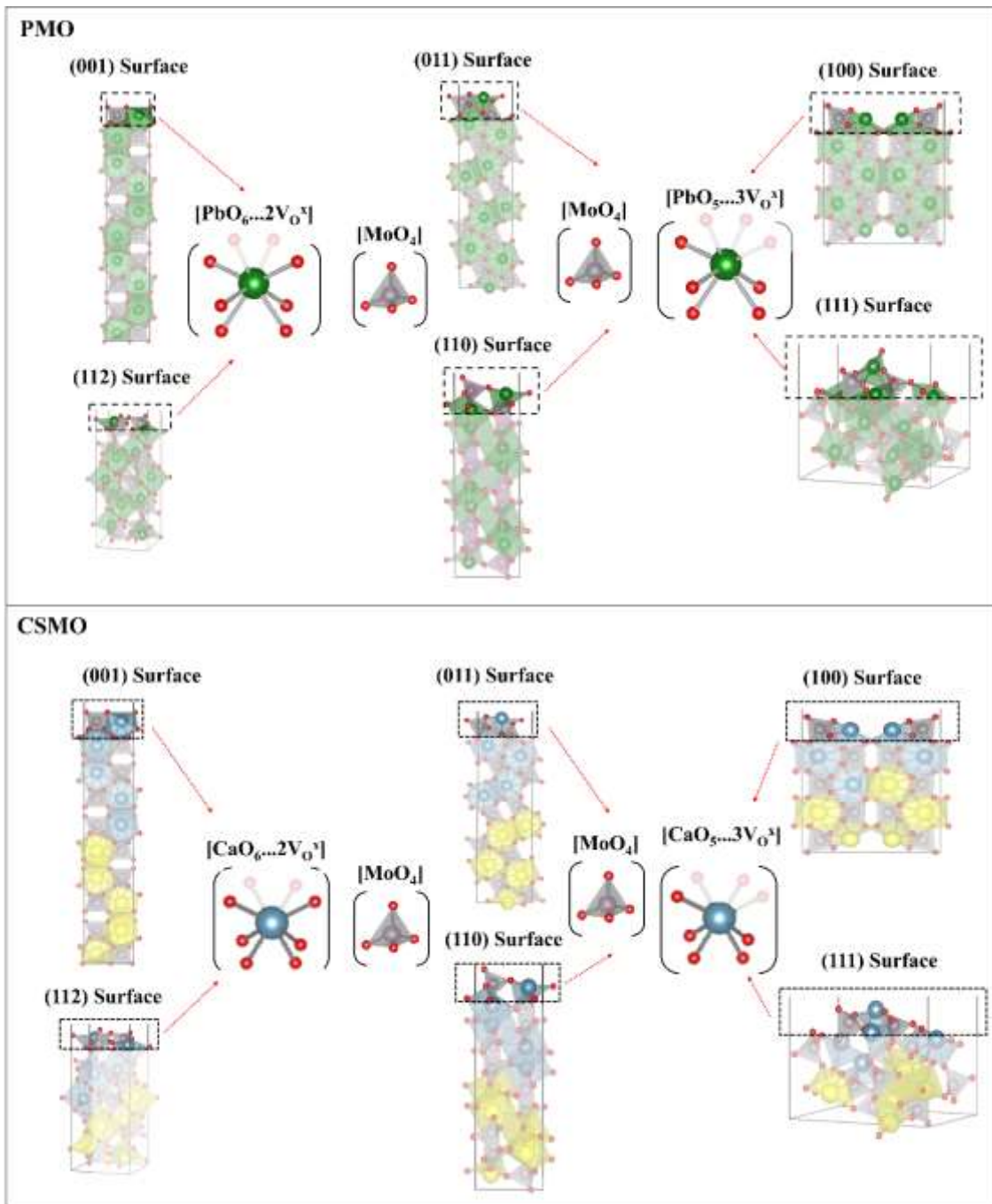
Figure 6. Schematic representations of surfaces: (001), (011), (110), (100), (111), and (112) for PMO and CSMO systems. The clusters and oxygen vacancies are written using the Kröger-Vink notation.
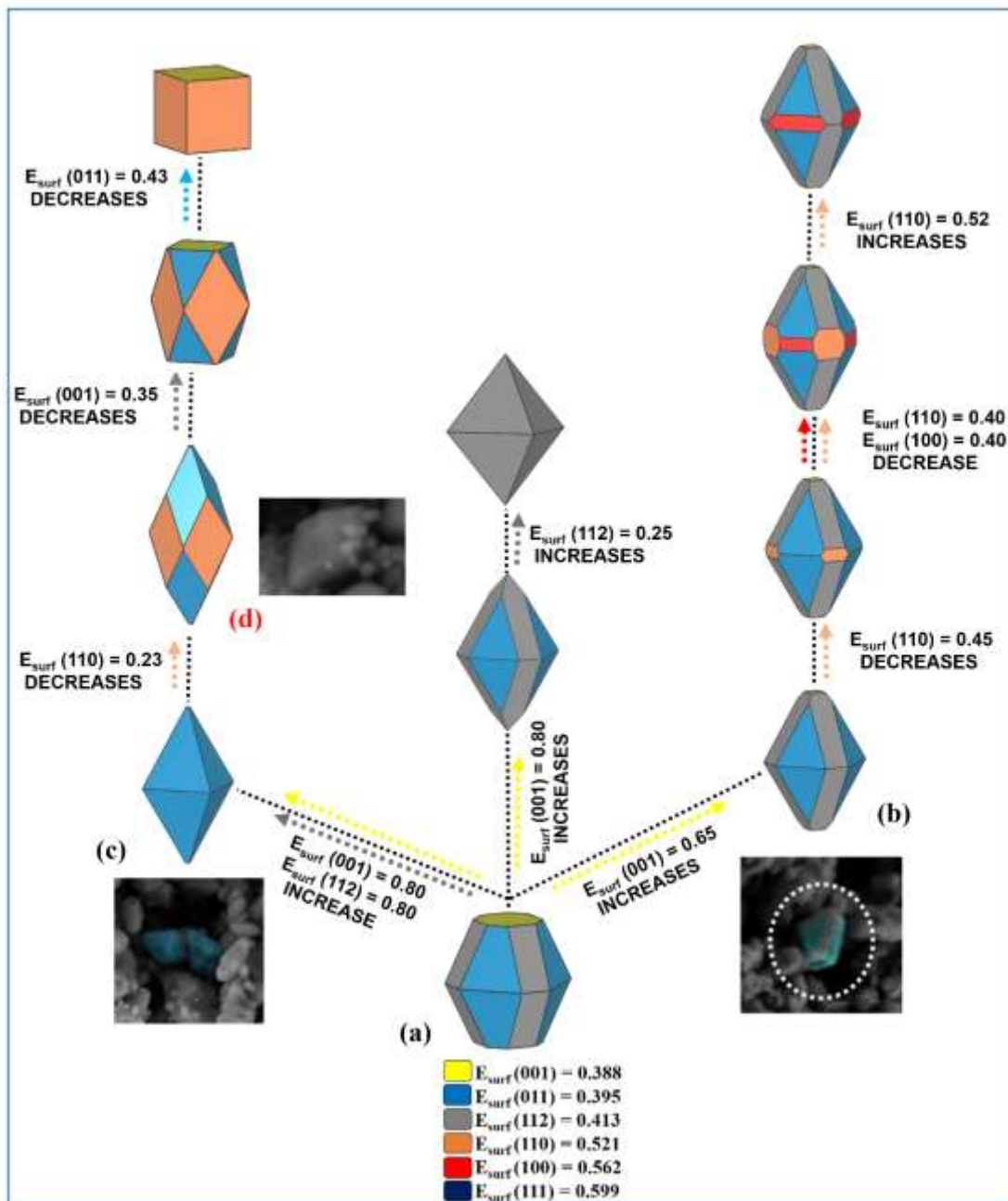
Figure 7. The available morphology map for the PMO crystals (E_{surf} are given in J/m^2). The experimental FE-SEM images (inset) are included for comparison purposes.
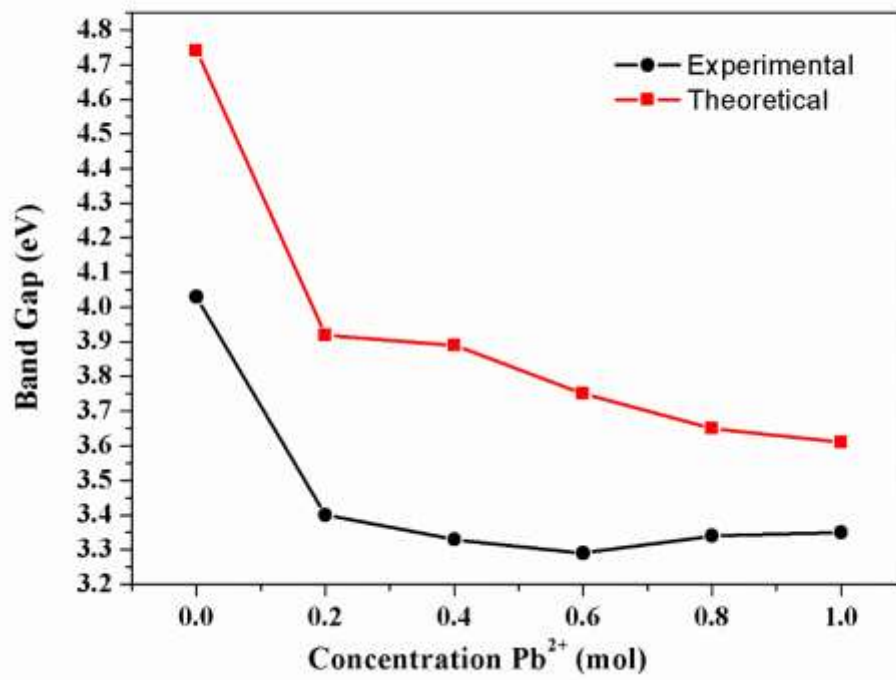
Figure 8. Experimental and theoretical variation of the E_{gap} values as a function of Pb content.
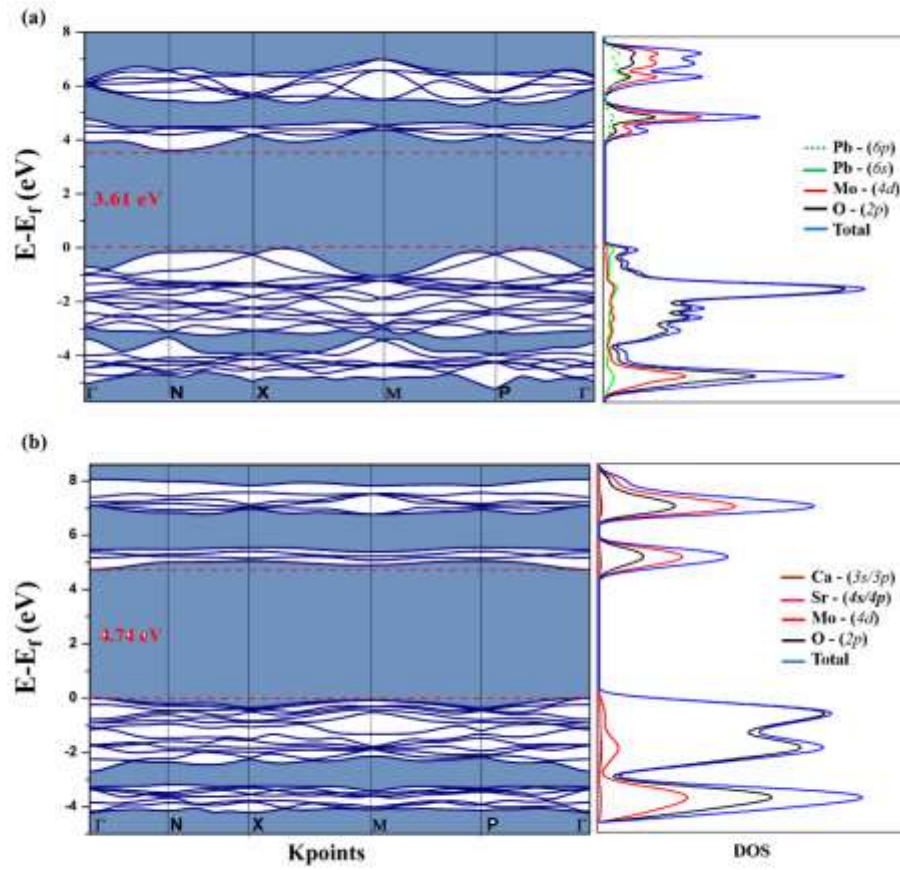
Figure 9. Calculated band structure and DOS projected on atoms of the Pb, Ca, Mo and O atoms in (a) PMO and (b) CSMO.
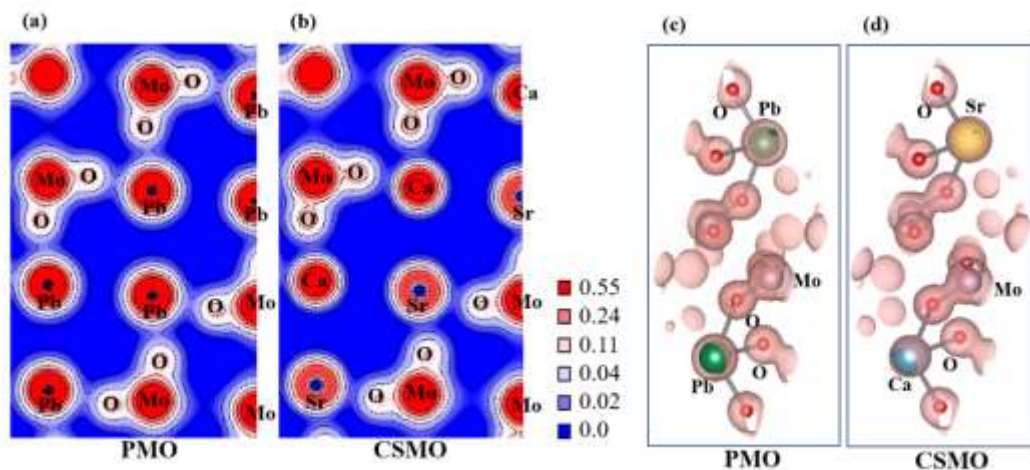
Figure 10. Electron density difference contour maps on the (100) plane (electron/bohr^3) for (a) PMO and (b) CSMO. High and low charge density values are shown in red and blue, respectively. The blue, white and red colors are 0.00, 0.11, and 0.55 electron/bohr^3, respectively. Electron density isosurfaces (electron /bohr^3) for PMO (c) and (d) CSMO.
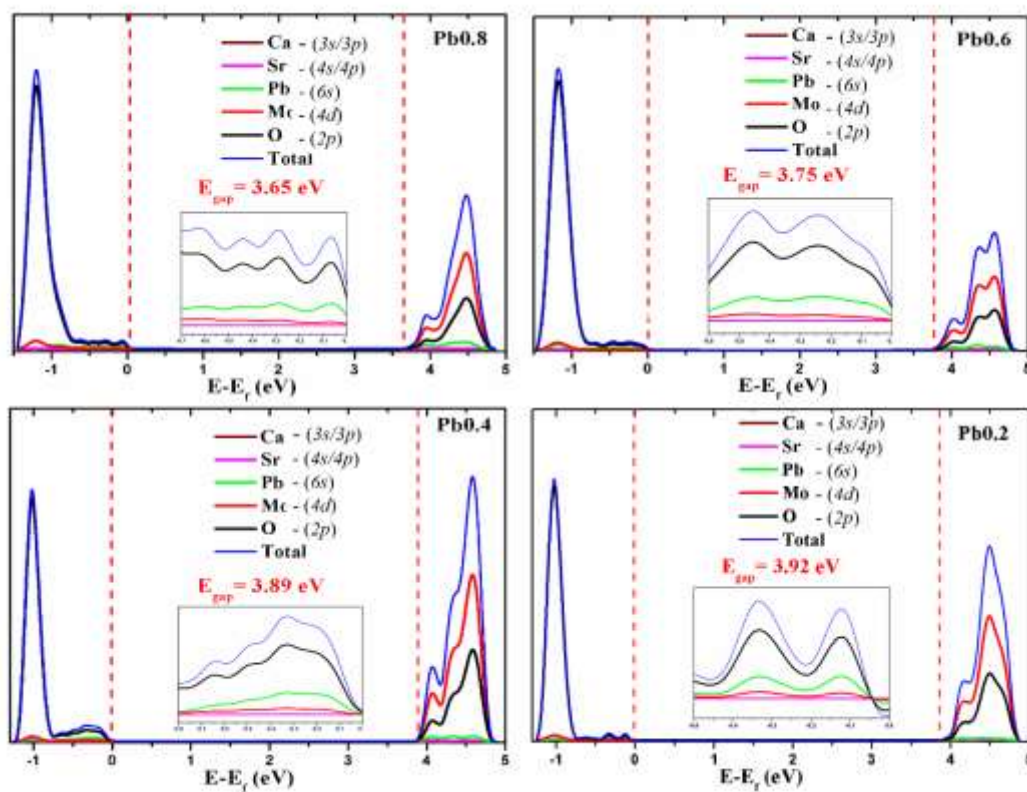

Figure 11. Calculated total DOS projected on atoms of the samples (a) Pb0.2, (b) Pb0.4, (c) Pb0.6, and (d) Pb0.8.
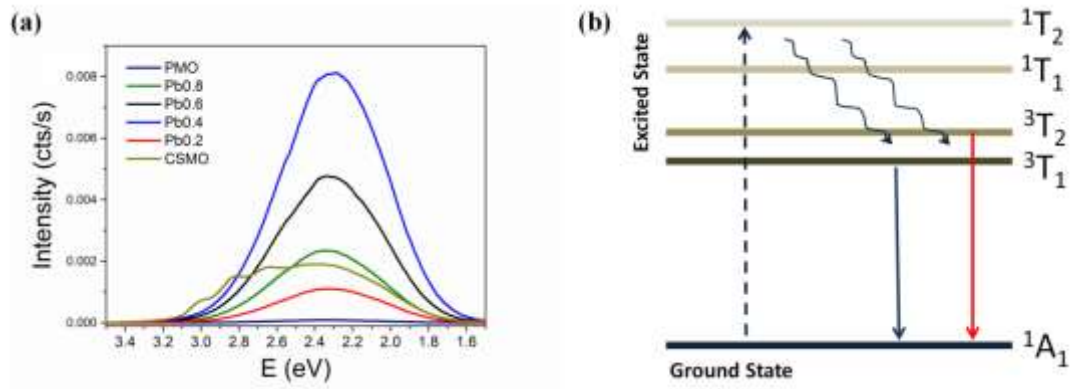
Figure 12. (a) PL emissions, (b) Schematic diagram of energetic levels of the fundamental, $^1A_1$, and excited, $^1T_2$, $^1T_1$, $^3T_2$, and $^3T_2$, electronic states for $[MoO_4]^{2-}$ anion. The intersystem crossing processes between singlet and triplet states are displayed.

Figure 13. A pictorial representation of the relationship between the PL emission energy and location of electronic states within the band gap for the (a) PMO, (b)Pb0.8 and (c) Pb0.6.

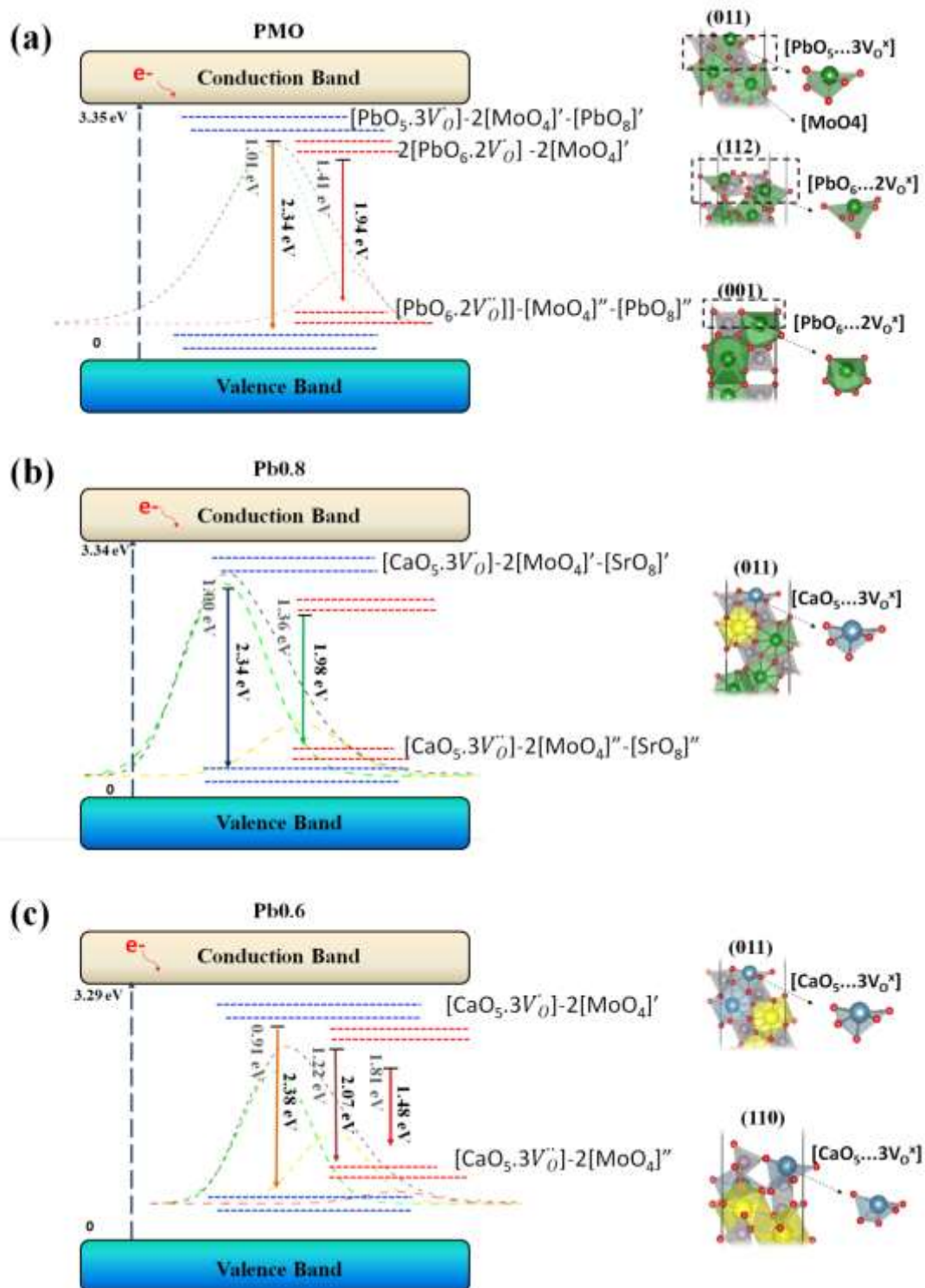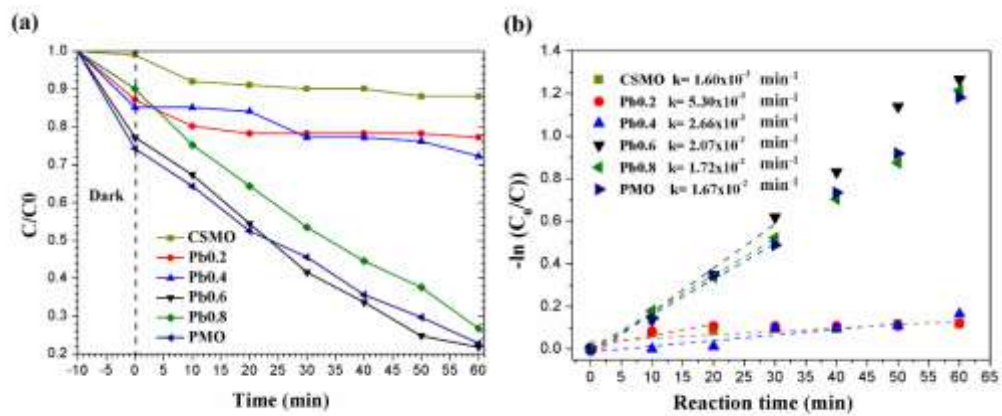**Figure 14.** Photocatalysis degradation profiles of RhB for PMO and solid solution samples: (a) Pb0.8, Pb0.6, Pb0.4, Pb0.2 and (b) CSMO Photocatalytic reaction kinetics.

Tables

Table 1. Experimental and theoretical values of lattice constants (a, b and c in Å), volume (V in $Å^3$), bond distances (Pb-O, Mo-O, Sr-O and Ca-O in Å), coordinates of the oxygen atom in Å and Rietveld refinement parameters of PMO and CSMO.

	Cell Parameters (Å)			
Samples	**PMO**		**CSMO**	
	Experimental	**Theoretical**	**Experimental**	**Theoretical**
a=b	5.432	5.529	5.328	5.390
C	12.117	12.234	11.785	11.882
Volume ($Å^3$)	357.574	374.061	334.681	345.234
Bond Distancies (Å)				
Pb-O	2.602 (x4)	2.638 (x4)		
	2.781 (x4	2.666 (x4)		
Mo-O	1.710 (x4)	1.811 (x4)	1.750 (x4)	1.807 (x4)
Sr-O			2.540 (x4)	2.572 (x4)
			2.570 (x4)	2.597 (x4)
Ca-O			2.540 (x4)	2.508 (x4)
			2.570 (x4)	2.536 (x4)
Coordinates of the oxygen atom (Å)				
X	0.2117	0.2376	0.2367	0.2426
Y	0.1247	0.1127	0.1115	0.1016
Z	0.0370	0.4408	0.0434	0.0444
Rietveld Parameters				
X^2	3.365		2.075	
R (%)	20.820		16.520	
Rp (%)	15.720		12.900	

Table 2. Experimental and theoretical values of lattice constants (a, b and c in Å), volume (V in Å^3), bond distances (Pb-O, Mo-O, Sr-O and Ca-O, in Å), coordinates of the oxygen atom in Å and Rietveld refinement parameters of $Pb_{1-2x}Ca_xSr_xMoO_4$ solid solutions.

	PMO and Solid solutions ($Pb_{1-2x}Ca_xSr_xMoO_4$; x= 0.1, 0.2, 0.3, 0.4)								
Samples	**PMO (x=0)**	**Pb0.8 (x=0.1)**		**Pb0.6 (x=0.2)**		**Pb0.4 (x=0.3)**		**Pb0.2 (x=0.4)**	
	Theoretical	**Experimental**	**Theoretical**	**Experimental**	**Theoretical**	**Experimental**	**Theoretical**	**Experimental**	**Theoretical**
a=b	5.529	5.425	5.499	5.429	5.467	5.428	5.439	5.429	5.409
c	12.234	12.092	12.173	12.091	12.110	12.085	12.043	12.099	11.970
Volume (Å^3)	374.061	356.001	368.427	356.385	362.740	356.086	357.010	356.720	351.152
Bond distancies (Å)									
Pb-O	2.638 (x4)	2.603 (4x)	2.599-2.661*	2.680 (x4)	2.583-2.660*	2.760 (x4)	2.571-2.656*	2.622 (x4)	2.556-2.652*
	2.666 (x4)	2.708 4x)		2.696 (x4)		2.770 (x4)		2.713 (x4)	
Mo-O	1.811 (x4)	1.723 (4x)	1.805-1.811*	1.649 (x4)	1.809-1.814*	1.530 (x4)	1.809-1.816*	1.711 (x4)	1.806-1.811*
Ca-O			2.493-2.554*		2.488-2.559*		2.491-2.541*		2.500-2.539*
Sr-O			2.598-2.637*		2.587-2.638*		2.574-2.633*		2.562-2.631*
Coordinates of the oxygen atom (Å)									
X	0.2376	0.2254	0.2380	0.2229	0.2388	0.2080	0.2397	0.2219	0.2406
Y	0.1127	0.1237	0.1120	0.1250	0.1102	0.1380	0.1075	0.1223	0.1048
Z	0.0441	0.0422	0.0441	0.0513	0.0442	0.0552	0.0442	0.0426	0.0443
Parameters Rietveld									
X^2		2.613		1.621		1.465		1.432	
Rp		15.20		11.32		10.67		9.8	
R$_{wp}$		19.60		15.70		14.10		13.15	

Note: * Range of values for each bond distance.